Fractal energy gaps and topological invariants in hBN/graphene/hBN double moiré systems

Hiroki Oka and Mikito Koshino
Department of Physics, Osaka University, Osaka 560-0043, Japan

We calculate the electronic structure in quasiperiodic double moiré systems of graphene sandwiched by hexagonal boron nitride (hBN) and identify the characteristic integers of energy gaps. We find that the electronic spectrum contains a number of minigaps, and they exhibit a recursive fractal structure similar to the Hofstadter butterfly when plotted against the twist angle. Each of the energy gaps can be characterized by a set of integers, which are associated with an area in momentum space. The corresponding area is geometrically interpreted as a quasi-Brillouin zone, which is a polygon enclosed by multiple Bragg planes of the composite periods and can be uniquely specified by the plain wave projection in the weak-potential limit.

I. INTRODUCTION

In twisted multilayers of two-dimensional (2D) materials, the moiré interference pattern causes the electronic band reconstruction, leading to unusual physical properties highly tunable by the twist angle. The best-known example is twist bilayer graphene [1–8], where the flat band formation at the magic angle gives rise to exotic phenomena [9–12]. The superlattice of graphene on hexagonal boron nitride (hBN) has also been extensively studied [13–22], where the moiré potential creates the superlattice subbands in the Dirac cone.

Recently, attention has also been paid to systems where multiple moiré superperiods compete. The hBN/graphene/hBN stack [23–30] is a typical example, where the moiré pattern caused by graphene and the upper hBN layer and that caused by graphene and the lower hBN layer form an incommensurate doubly periodic potential to graphene, as shown in Fig. 1(a). A similar situation is also found in twisted bilayer graphene on hBN [31–33] and in twisted trilayer graphene. [34–37]

The hBN/graphene/hBN system is realized when monolayer graphene is encapsulated by top and bottom hBN substrates. There the dual moiré effect is relevant only when the lattice orientations of the upper and lower hBN layers are nearly aligned to graphene since, otherwise, the moiré wavelength is too short and hardly affects the low-energy electronic states of graphene. Nearly aligned hBN/graphene/hBN superlattices were experimentally fabricated using various techniques, [23–26,29,30], and it was shown that the coexistence of the different superperiods gives rise to multiple minigaps in the spectrum, which can never be seen in a single moiré potential [24,25].

Theoretically, double moiré systems are generally hard to treat because the two superlattice periods are incommensurate in general and then the Hamiltonian is essentially quasiperiodic. The band structure of the hBN/graphene/hBN system was calculated using large-scale numerical simulations [27,28], where several major gaps and pseudogaps were found as traces in the energy spectrum against the twist angle.

Here we ask, How can we characterize energy gaps in quasiperiodic systems? In a periodic system, the electronic spectrum is separated into Bloch subbands accommodating equal electron density, and the number of subbands below a given gap is a topological invariant of zero dimension defined for the Hamiltonian at a single Bloch wave number [38–40]. In a doubly periodic system, however, the absence of the rigorous unit cell prevents the definition of the Brillouin zone, so the integer characterization is not obvious. In one dimension, an energy gap in a double period with wave numbers G^α and G^β is characterized by a pair of integers p and q, where the electron density below the gap is given by $n_e = (pG^\alpha + qG^\beta)/(2\pi)$. This is regarded as the Bragg gap of the $(|p| + |q|)$th-order harmonics. The integers p and q are directly related to the topological properties such as adiabatic pumping [41–44] and the quantum Hall effect [45]. In the hBN/graphene/hBN system, similarly, some of the gaps can be associated with the Bragg gap of a composite reciprocal lattice vector, $p\mathbf{G}_1^\alpha + q\mathbf{G}_2^\alpha + r\mathbf{G}_1^\beta + s\mathbf{G}_2^\beta$, where indexes α, β label the two different moiré patterns [24,25,27,28]. This scheme successfully explains a few gaps in the low-energy region but does not generally work for all the gaps in the spectrum.

In this paper, we calculate the electronic structure of the hBN/graphene/hBN system in changing the twist angle and identify the characteristic integers of all the energy gaps by using a different scheme. First, we compute the band structures for a series of the commensurate approximants to simulate a continuous change in the twist angle. We find that the electronic spectrum actually contains a number of minigaps, exhibiting a recursive fractal structure when plotted against the twist angle. The integer characterization for the energy gaps is employed as follows. The system has four distinct reciprocal lattice vectors $\mathbf{G}_1^\alpha, \mathbf{G}_2^\alpha, \mathbf{G}_1^\beta, \mathbf{G}_2^\beta$, and we can define a momentum space area element $(\mathbf{G}_i^\lambda \times \mathbf{G}_j^\mu)_z$ by taking the cross product of two distinct vectors. As a result, we have four linearly independent areas $A_1, \dots, A_4$, as shown in Fig. 2(a), which can be viewed as projected areas of the four-dimensional hypercube. We find that each
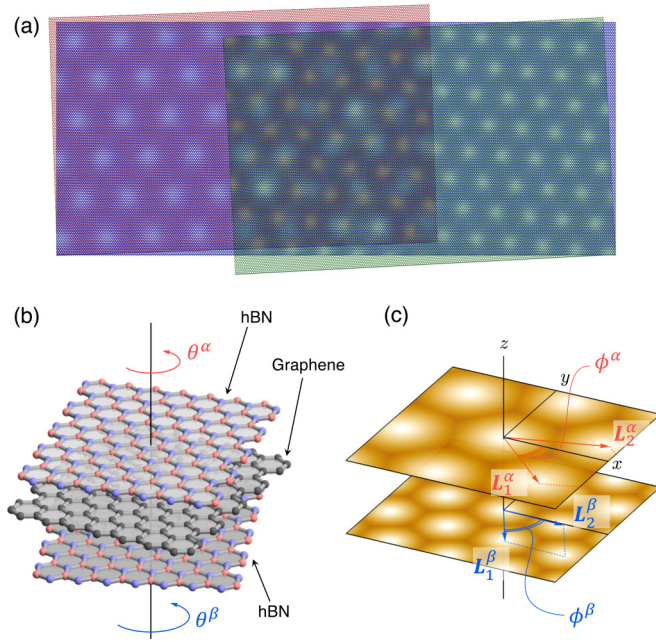
FIG. 1. (a) Incommensurate moiré structure in the trilayer system. (b) The atomic model of the hBN/graphene/hBN trilayer system. Top and bottom hBN layers are stacked with twist angles θ^α and θ^β from the middle graphene layer. (c) Top and bottom moiré patterns. The moiré superlattice vector depends on the twist angle, and the moiré angle ϕ increases as the twist angle increases.

energy gap is characterized by a set of integers $m_1, \ldots, m_4$ such that the electron density below the gap is given by $n_e = \sum_i m_i A_i/(2\pi)^2$. Moreover, we show that the area $\sum_i m_i A_i$ is geometrically interpreted as a quasi-Brillouin zone, which is a certain polygon composed of multiple Bragg-plane segments, as shown in Fig. 2(b). The quasi-Brillouin zone for a given gap can be identified by the plain wave projection in the weak-potential limit. The band-gap characterization proposed in this work would be useful in other quasiperiodic 2D systems, such as twisted trilayer graphene, the twisted bilayer graphene on hBN mentioned above, and also 30° twisted bilayer graphene [46–49].

This paper is organized as follows. In Sec. II, we define the commensurate approximants and introduce the effective continuum Hamiltonian for the hBN/graphene/hBN system. We calculate the energy spectrum in Sec. III A and specify the characteristic integers of the band gaps in Sec. III B. In Sec. III C, we identify the quasi-Brillouin zone associated with the characteristic integers by using the plain wave projection. A brief conclusion is given in Sec. IV.

II. METHOD

A. Atomic structure

We consider a hBN/graphene/hBN trilayer system, as illustrated in Fig. 1, where the top ($\lambda = \alpha$) and bottom ($\lambda = \beta$) hBN layers are rotated by θ^α and θ^β, respectively, relative to the middle graphene layer. Graphene and hBN share the same honeycomb structure with different lattice constants, $a \approx 0.246$ nm and $a_{\text{hBN}} \approx 0.2504$ nm, respectively [50]. We define A and B as sublattices for graphene and A^λ and B^λ as
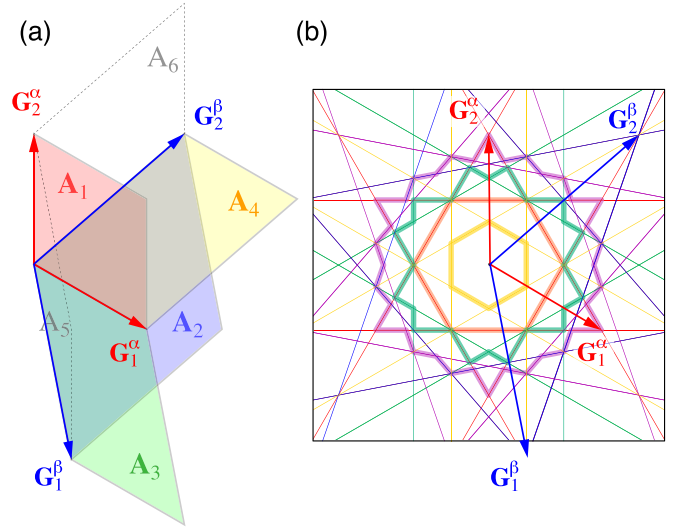

FIG. 2. (a) Independent unit area elements A_1, A_2, A_3, A_4 obtained by the cross product of the reciprocal lattice vectors $\mathbf{G}_1^\alpha, \mathbf{G}_2^\alpha, \mathbf{G}_1^\beta, \mathbf{G}_2^\beta$ in the hBN/graphene/hBN double moiré system [Eq. (19)]. A_5 and A_6 (dashed areas) can be expressed by other elements as $A_5 = -A_3 - A_4$ and $A_6 = A_3$. (b) Example of the quasi-Brillouin zone (thick lines), which is composed of the Bragg planes for composite reciprocal lattice vectors (thin lines). See Fig. 8 for more details.

nitrogen and boron sites of the λth hBN layer, respectively. The geometry $\theta^\lambda = 0$ is defined by the AB bond and the $A^\lambda B^\lambda$ bond being parallel to each other.

The lattice vectors of graphene are given by $\mathbf{a}_1 = a(1, 0)$ and $\mathbf{a}_2 = a(1/2, \sqrt{3}/2)$, and those of hBN layers of $\lambda = \alpha, \beta$ are given by

$$\mathbf{a}_i^\lambda = MR(\theta^\lambda)\mathbf{a}_i \quad (i = 1, 2), \tag{1}$$

where $R(\theta^\lambda)$ is the 2D rotation matrix of θ^λ and $M = (1 + \varepsilon)\mathbf{1}$ represents the isotropic expansion by the factor $1 + \varepsilon = a_{\text{hBN}}/a \approx 1.018$. In the following, we assume the twist angles θ^α and θ^β are small enough (a few degree or less) that the moiré superperiod is much greater than the atomic lattice constant a. The primitive lattice vectors of the moiré pattern of layer l are given by [18,51]

$$\mathbf{L}_i^\lambda = [\mathbf{1} - R(\theta^\lambda)^{-1}M^{-1}]^{-1}\mathbf{a}_i \quad (i = 1, 2). \tag{2}$$

The corresponding reciprocal lattice vectors are

$$\mathbf{G}_i^\lambda = [\mathbf{1} - M^{-1}R(\theta^\lambda)]\mathbf{a}_i^* \quad (i = 1, 2), \tag{3}$$

where $\mathbf{a}_i^*$ is the reciprocal lattice vectors for graphene which satisfy $\mathbf{a}_i \cdot \mathbf{a}_j^* = 2\pi\delta_{ij}$.

The moiré superlattice period is given by

$$\left|\mathbf{L}_1^\lambda\right| = \left|\mathbf{L}_2^\lambda\right| = \frac{1 + \varepsilon}{\sqrt{\varepsilon^2 + 2(1 + \varepsilon)(1 - \cos\theta^\lambda)}} a. \tag{4}$$

The moiré rotation angle, or the relative angle of $\mathbf{L}_i^\lambda$ to $\mathbf{a}_i$, is given by

$$\phi^\lambda = \arctan\left(\frac{-\sin\theta^\lambda}{1 + \varepsilon - \cos\theta^\lambda}\right). \tag{5}$$

Figures 3(a) and 3(b) plot the moiré superlattice period L and the moiré rotation angle ϕ as a function of the twist angle θ,
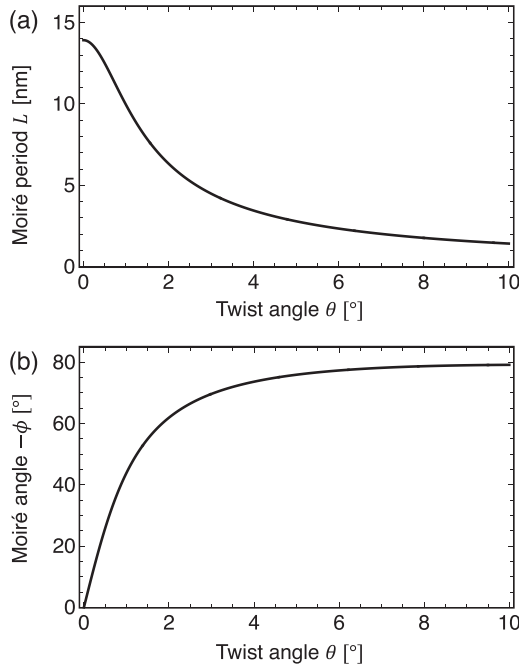
FIG. 3. (a) Moiré period L [Eq. (4)] and (b) the moiré rotation angle ϕ [Eq. (5)] as a function of the twist angle θ.

respectively. The superperiod L is ~ 13.9 nm at $\theta = 0°$, and it decreases with increasing θ. The rotation angle ϕ is zero at $\theta = 0$ and rapidly increases in the negative direction with increasing θ.

B. Commensurate moiré approximation

Generally, the two moiré superperiods of α and β are incommensurate, and hence, there is no unit cell in the trilayer systems as a whole. In any $(\theta^\alpha, \theta^\beta)$, however, we always have a certain pair of lattice points of the two moiré patterns which happen to be very close to each other. The situation is expressed as

$$n_1^\alpha \boldsymbol{L}_1^\alpha + n_2^\alpha \boldsymbol{L}_2^\alpha = n_1^\beta \boldsymbol{L}_1^\beta + n_2^\beta \boldsymbol{L}_2^\beta + \Delta \mathbf{L}, \quad (6)$$

where n_j^λ are integers and $\Delta \mathbf{L}$ is the difference. When $\Delta \mathbf{L}$ is much smaller than the moiré periods, the electronic structure of such a system can be approximated by an exactly commensurate system with $\Delta \mathbf{L}$ neglected. Specifically, it is obtained by slightly rotating and expanding or shrinking the moiré patterns so that $\Delta \mathbf{L}$ vanishes. Figure 4(a) shows an actual example of the commensurate approximant for $(\theta^\alpha, \theta^\beta) = (0, 1.1908°)$, where $(n_1^\alpha, n_2^\alpha) = (1, 1)$ and $(n_1^\beta, n_2^\beta) = (-1, 3)$.

When $\Delta \mathbf{L}$ is neglected, Eq. (6) gives a primitive lattice vector of the commensurate supermoiré structure $\boldsymbol{L}_1^{\mathrm{SM}}$ (SM stands for supermoiré). The other primitive vector $\boldsymbol{L}_2^{\mathrm{SM}}$ is obtained by rotating $\boldsymbol{L}_1^{\mathrm{SM}}$ by 60°. As a result, we have

$$\begin{pmatrix} \boldsymbol{L}_1^{\mathrm{SM}} \\ \boldsymbol{L}_2^{\mathrm{SM}} \end{pmatrix} = \begin{pmatrix} n_1^\alpha & n_2^\alpha \\ -n_2^\alpha & n_1^\alpha + n_2^\alpha \end{pmatrix} \begin{pmatrix} \boldsymbol{L}_1^\alpha \\ \boldsymbol{L}_2^\alpha \end{pmatrix}$$

$$= \begin{pmatrix} n_1^\beta & n_2^\beta \\ -n_2^\beta & n_1^\beta + n_2^\beta \end{pmatrix} \begin{pmatrix} \boldsymbol{L}_1^\beta \\ \boldsymbol{L}_2^\beta \end{pmatrix}. \quad (7)$$
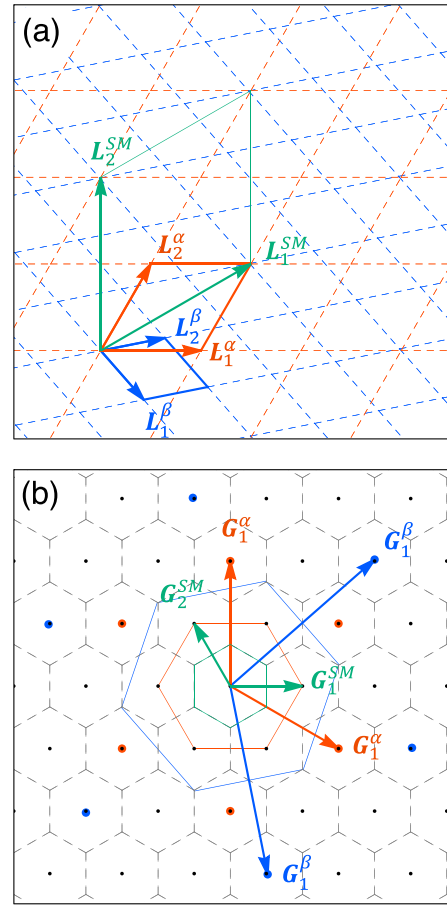

FIG. 4. (a) Supermoiré unit cell and (b) the corresponding reciprocal lattice of the commensurate approximant for $(\theta^\alpha, \theta^\beta) = (0, 1.1908°)$, where $(n_1^\alpha, n_2^\alpha) = (1, 1)$ and $(n_1^\beta, n_2^\beta) = (-1, 3)$.

Correspondingly, the reciprocal superlattice vectors $\boldsymbol{G}_1^{\mathrm{SM}}, \boldsymbol{G}_2^{\mathrm{SM}}$ are given by

$$\begin{pmatrix} \boldsymbol{G}_1^{\mathrm{SM}} \\ \boldsymbol{G}_2^{\mathrm{SM}} \end{pmatrix} = \begin{pmatrix} n_1^\alpha & -n_2^\alpha \\ n_2^\alpha & n_1^\alpha + n_2^\alpha \end{pmatrix}^{-1} \begin{pmatrix} \boldsymbol{G}_1^\alpha \\ \boldsymbol{G}_2^\alpha \end{pmatrix}$$

$$= \begin{pmatrix} n_1^\beta & -n_2^\beta \\ n_2^\beta & n_1^\beta + n_2^\beta \end{pmatrix}^{-1} \begin{pmatrix} \boldsymbol{G}_1^\beta \\ \boldsymbol{G}_2^\beta \end{pmatrix}. \quad (8)$$

Figure 4(b) is the reciprocal lattice corresponding to Fig. 4(a).

In the following, we consider two series of hBN/graphene/hBN trilayer systems,

$$\begin{aligned} \mathrm{I}: \quad & (\theta^\alpha, \theta^\beta) = (0, \theta), \qquad 0 \leqslant \theta \leqslant 2°, \\ \mathrm{II}: \quad & (\theta^\alpha, \theta^\beta) = (\theta, -\theta), \qquad 0 \leqslant \theta \leqslant 2°. \end{aligned} \quad (9)$$

In each case, we find a set of $(\theta^\alpha, \theta^\beta)$ satisfying that $\Delta \mathbf{L}$ is less than 1% of $|n_1^\alpha \boldsymbol{L}_1^\alpha + n_2^\alpha \boldsymbol{L}_2^\alpha|$ and $n_1^\alpha, n_2^\alpha \leqslant n_{\max}$, where $n_{\max} = 12$ and 17 for series I and II, respectively. The full list of $(\theta^\alpha, \theta^\beta)$ in series I (II) is presented in Table I (Table II) in the Appendix. In series II, the list is dominated by exactly commensurate systems (i.e., $\Delta \mathbf{L} = 0$) which appear when the moiré periods of α and β are equal. For later reference, we label those commensurate cases by

$[(n_1^\alpha, n_2^\alpha), (n_1^\beta, n_2^\beta)]$ as

$$p_{mn} \equiv [(m, n), \ (n, m)],$$

$$q_{mn} \equiv [(m, n), \ (m + n, -n)],$$

$$r_{mn} \equiv [(m, n), \ (m, -m - n)]. \quad (10)$$

C. Effective Hamiltonian

Since the hBN has a semiconducting gap, the low-energy spectrum of the hBN/graphene/hBN system is dominated by the Dirac cones of graphene. We can derive the continuum Hamiltonian of the trilayer system in a manner similar to that for the graphene-hBN bilayer [14–22]. It is written in 6×6 matrix form as

$$H_{\text{eff}} = \begin{pmatrix} H_G & U^{\alpha\dagger} & U^{\beta\dagger} \\ U^\alpha & H_{\text{hBN}} & 0 \\ U^\beta & 0 & H_{\text{hBN}} \end{pmatrix}, \quad (11)$$

which works on the basis of $\{A, B, A^\alpha, B^\alpha, A^\beta, B^\beta\}$. H_G (2×2 matrix) is the Hamiltonian for graphene, which is given by

$$H_G \approx -\hbar v \mathbf{k} \cdot \boldsymbol{\sigma}_\xi, \quad (12)$$

where $\xi = \pm 1$ is the valley index of graphene which corresponds to the wave point $\mathbf{K}_\xi = -\xi(2\mathbf{a}_1^* + \mathbf{a}_2^*)/3$, $\mathbf{k}$ is the relative wave number measured from the $\mathbf{K}_\xi$ point, and $\boldsymbol{\sigma}_\xi = (\xi\sigma_x, \sigma_y)$, with Pauli matrices σ_x and σ_y. H_{hBN} in the second and third diagonal blocks is the Hamiltonian for monolayer hBN. Here we adopt an approximation considering only the on-site potential [14,18],

$$H_{\text{hBN}} \approx \begin{pmatrix} V_N & 0 \\ 0 & V_B \end{pmatrix}. \quad (13)$$

The off-diagonal matrix U^λ is the interlayer Hamiltonians of the twist angle θ^λ, given by [18]

$$U^\lambda = t_0 \left[\begin{pmatrix} 1 & 1 \\ 1 & 1 \end{pmatrix} + \begin{pmatrix} 1 & \omega^{-\xi} \\ \omega^\xi & 1 \end{pmatrix} e^{i\xi \mathbf{G}_1^\lambda \cdot (\mathbf{r} - \mathbf{r}_0^\lambda)} \right.$$

$$\left. + \begin{pmatrix} 1 & \omega^\xi \\ \omega^{-\xi} & 1 \end{pmatrix} e^{i\xi(\mathbf{G}_1^\lambda + \mathbf{G}_2^\lambda) \cdot (\mathbf{r} - \mathbf{r}_0^\lambda)} \right], \quad (14)$$

where $t_0 \approx 150$ meV is the interlayer coupling energy and $\mathbf{r}_0^\lambda$ is the origin of the moiré pattern of layer λ, which can be changed by sliding the hBN layer relative to graphene [44].

The low-energy effective Hamiltonian for graphene can be obtained by eliminating the hBN bases by the second-order perturbation. It is explicitly written as

$$H_G^{(\text{eff})} = H_G + V_{\text{hBN}}^\alpha + V_{\text{hBN}}^\beta, \quad (15)$$

where

$$V_{\text{hBN}}^\lambda \equiv U^{\lambda\dagger}(-H_{\text{hBN}})^{-1}U^\lambda$$

$$= V_0 \begin{pmatrix} 1 & 0 \\ 0 & 1 \end{pmatrix} + \left\{ V_1 e^{i\xi\psi} \left[\begin{pmatrix} 1 & \omega^{-\xi} \\ 1 & \omega^{-\xi} \end{pmatrix} e^{i\xi \mathbf{G}_1^\lambda \cdot (\mathbf{r} - \mathbf{r}_0^\lambda)} \right.\right.$$

$$+ \begin{pmatrix} 1 & \omega^\xi \\ \omega^\xi & \omega^{-\xi} \end{pmatrix} e^{i\xi \mathbf{G}_2^\lambda \cdot (\mathbf{r} - \mathbf{r}_0^\lambda)}$$

$$\left.\left. + \begin{pmatrix} 1 & 1 \\ \omega^{-\xi} & \omega^{-\xi} \end{pmatrix} e^{i\xi \mathbf{G}_3^\lambda \cdot (\mathbf{r} - \mathbf{r}_0^\lambda)} \right] + \text{H.c.} \right\}, \quad (16)$$

with

$$V_0 = -3t_0^2 \left(\frac{1}{V_N} + \frac{1}{V_B} \right), \quad (17)$$

$$V_1 e^{i\psi} = -t_0^2 \left(\frac{1}{V_N} + \omega \frac{1}{V_B} \right), \quad (18)$$

and $\mathbf{G}_3^\lambda = -\mathbf{G}_1^\lambda - \mathbf{G}_2^\lambda$, $V_0 \approx 29$ meV, $V_1 \approx 21$ meV, and $\psi \approx -0.29$ rad [18].

Using the effective Hamiltonian in Eq. (11), we calculate the band structure of the approximate commensurate systems introduced in the previous section. The set of wave numbers hybridized by the commensurate double moiré pattern is given by $\mathbf{q}_{m_1,m_2} = \mathbf{k} + m_1 \mathbf{G}_1^{\text{SM}} + m_2 \mathbf{G}_2^{\text{SM}}$, where m_1 and m_2 are integers and $\mathbf{k}$ is a residual wave number defined inside the first supermoiré Brillouin zone spanned by $\mathbf{G}_1^{\text{SM}}$ and $\mathbf{G}_2^{\text{SM}}$. We construct the Hamiltonian matrix in the bases for graphene, $\{|\mathbf{q}_{m_1,m_2}, A\rangle, |\mathbf{q}_{m_1,m_2}, B\rangle\}$, with k-space cutoff $|\mathbf{q}_{m_1,m_2}| < q_c$. Here we take $q_c = 2|\mathbf{G}_1^\beta|$, which is about 0.54 eV for $\theta^\beta = 0°$ and 1.2 eV for $\theta^\beta = 2°$. Finally, the band diagram is obtained by plotting the eigenvalues of the Hamiltonian matrix as a function of $\mathbf{k}$.

III. RESULTS

A. Electronic spectrum

As a typical example, we show the band structure of the commensurate approximant for $(\theta^\alpha, \theta^\beta) = (0, 1.1908°)$, which is considered in Fig. 4. Here we set the origins of the moiré potentials $\mathbf{r}_0^\alpha, \mathbf{r}_0^\beta$ to zero. Figure 5(d) shows the energy band plotted along the symmetric line of the supermoiré Brillouin zone. For comparison, we also present the band structures with no moiré potential [intrinsic graphene; Fig. 5(a)], with only the top moiré potential [Fig. 5(b)], and with only the bottom moiré potential plotted on the same path [Fig. 5(c)]. In all the panels, we set the origin of energy (vertical axis) at the Dirac point of graphene. In the single moiré systems in Figs. 5(b) and 5(c), the biggest gap in the valence band (red and blue regions) is the first-order moiré gap corresponding to the electron density of one electron (per valley and per spin) for a moiré unit cell. In the double moiré system, on the other hand, we see a series of the higher-order gaps (green) due to the coexistence of the different moiré periods.

To study the twist-angle dependence of the electronic spectrum, we perform band calculations for all the systems in series I and II [Eq. (9)]. In any commensurate system, the band structure generally depends on the relative translation of the moiré potentials, $\Delta\mathbf{r}_0 = \mathbf{r}_0^\alpha - \mathbf{r}_0^\beta$. The dependence on $\Delta\mathbf{r}_0$ is generally greater in systems with smaller L_{SM}, and it quickly vanishes with increasing L_{SM}. As we see below, the gap structure as a function the twist angle becomes continuous only after the average over Δr_0 is taken at each angle. The reason is as follows: Let us consider a commensurate system A and an incommensurate system B generated by infinitesimally rotating system A. Now system B is regarded as a collection of all possible relative translations in A, just as a twisted bilayer graphene contains all the stacking structures of the nonrotated bilayer, such as the AA stack, AB stack, etc. Therefore, the
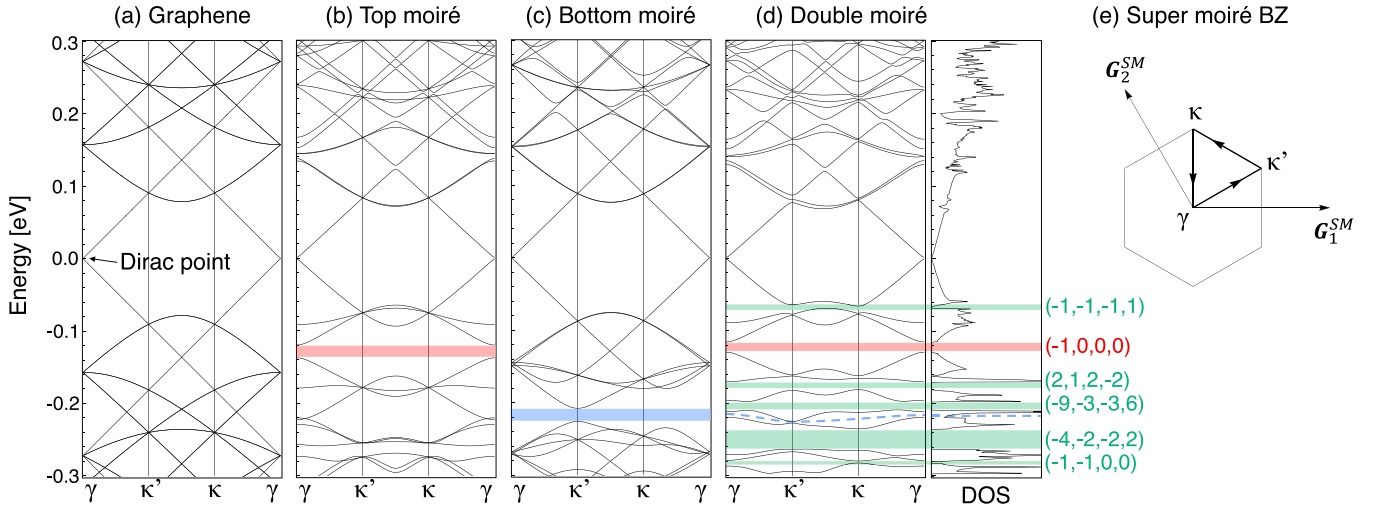
FIG. 5. Band structure of $(\theta^\alpha, \theta^\beta) = (0°, 1.1908°)$. (d) shows the energy band of the full double moiré potential plotted along the symmetric line of the supermoiré Brillouin zone shown in (e), with the corresponding DOS on the right. For comparison, we also show the energy bands with (a) no moiré potentials (intrinsic graphene), (b) only the top moiré potential, and (c) only the bottom moiré potential, plotted on the same path. The first-order gap of the top (bottom) moiré potential is colored red (blue), and the double moiré gaps are in green. The dashed blue curve in (d) is the position of the first-order gap of the bottom moiré potential, which actually does not open. The sets of numbers on the right indicate the characteristic integers (m_1, m_2, m_3, m_4) for energy gaps (see Sec. III B).

spectrum of B smoothly connects to that of A averaged over the relative translation. Here we average the density of states (DOS) over 25 grid points of $\Delta\mathbf{r}_0$ for systems with $L_{SM} < 50$ nm, and otherwise, we just take $\Delta\mathbf{r}_0 = 0$ since the dependence is minor.

Figure 6(a) shows a color map of the DOS calculated for series I $[(\theta^\alpha, \theta^\beta) = (0, \theta^\beta)]$, plotted against θ^β and energy. Here the brighter color indicates a larger DOS, and dark blue represents the gap. The array of bars at the top represents θ^β in series I (listed in Table I). The case $(\theta^\alpha, \theta^\beta) = (0, 1.1908°)$ considered in Fig. 5 is marked by the label (ii). Figure 6(c) shows the lower part of Fig. 6(a), where the first-order gaps of the single moiré pattern $\lambda = \alpha$ and β are highlighted by red and blue curves, respectively, and typical higher-order gaps are marked by green curves. Figure 6(b) is the corresponding map of the energy gaps with the vertical axis converted to the electron density, where the size of the black dots represents the gap width. In these plots, we see that the spectrum continuously changes as a function of the twist angle, even though the adjacent approximants in the series have completely different supermoiré periods and thus different numbers of minibands.

Figure 7 shows similar plots for series II plotted against $\theta^\alpha = -\theta^\beta$. The vertical lines labeled p_{mn}, q_{mn}, r_{mn} represent the commensurate angles defined in Eq. (10), and the numbers at the top (0, 30, . . . , 120) indicate $\phi^\beta - \phi^\alpha$, or the relative angle between the two moiré patterns. r_{10} ($\theta^\alpha \approx 0.5972°$) and q_{01} ($\theta^\alpha \approx 1.8377°$) are special cases where the relative angles of the two moiré patterns are 60° and 120°, respectively, and hence, the two moiré periods completely overlap. Here we have a relatively small number of the subbands because of the coincidence of the double period, but upon moving away from these angles, we see that a number of tiny levels branch out just like Landau levels in a magnetic field. As a whole, we observe a recursive pattern ruled by the commensurate lines such as $p_{n,n\pm1}, q_{n,n\pm1}, r_{n,n\pm1}$. The red dashed curves in Figs. 7(b) and 7(c) indicate the positions of the first-order gaps of the two

moiré patterns, which exactly match because $|\theta^\alpha| = |\theta^\beta|$. We observe that the first-order gap closes throughout Figs. 7(b) and 7(c) (dashed line), leaving only a small-DOS region. The reason for the absence of the first-order gap will be explained in the next section.

B. Characteristic integers for band gaps

The microgap structure observed in Figs. 6 and 7 resembles the Hofstadter butterfly [52], which is the energy spectrum of the 2D periodic lattice in magnetic field. The Hofstadter system is essentially equivalent to the one-dimensional (1D) Hamiltonian with a double period [53,54], where the fractal minigap structure emerges when the two periods are changed relative to each other. Each minigap is characterized by a pair of integers p and q, such that the electron density below the gap is given by $n_e = (pG^\alpha + qG^\beta)/(2\pi)$, where G^α and G^β are the wave numbers for the two periods. The present hBN/graphene/hBN system is a 2D version of this, where the double period is specified by $(\mathbf{G}_1^\alpha, \mathbf{G}_2^\alpha)$ and $(\mathbf{G}_1^\beta, \mathbf{G}_2^\beta)$. Actually, as shown in the following, all the gaps observed in Figs. 6 and 7 can be uniquely characterized by *four* integers associated with a specific k-space region.

Let us consider a general situation where the two moiré patterns are incommensurate. We can define four independent unit areas by combining the four independent reciprocal lattice vectors $\mathbf{G}_1^\alpha, \mathbf{G}_2^\alpha, \mathbf{G}_1^\beta, \mathbf{G}_2^\beta$ as

$$A_1 = \left(\mathbf{G}_1^\alpha \times \mathbf{G}_2^\alpha\right)_z, \quad A_2 = \left(\mathbf{G}_1^\beta \times \mathbf{G}_2^\beta\right)_z,$$
$$A_3 = \left(\mathbf{G}_1^\alpha \times \mathbf{G}_1^\beta\right)_z, \quad A_4 = \left(\mathbf{G}_1^\alpha \times \mathbf{G}_2^\beta\right)_z, \quad (19)$$

which are illustrated in Fig. 2(a). Here $(\cdots)_z$ represents the z component perpendicular to the plane, and it can be negative depending on the relative angles between the two vectors. A_1 and A_2 are the Brillouin zone areas of the individual moiré patterns of $\lambda = \alpha$ and β, respectively, while A_3 and A_4 are cross
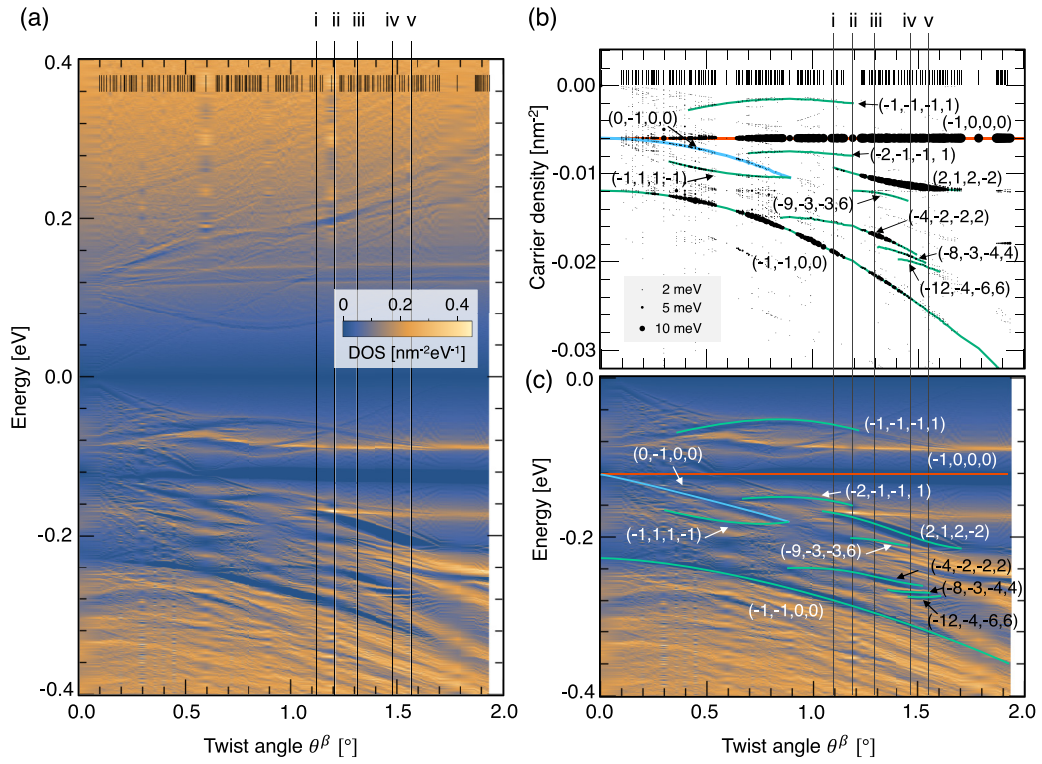
FIG. 6. (a) Color map of the density of states (DOS) of series I $[(\theta^\alpha, \theta^\beta) = (0, \theta^\beta)]$, plotted against θ^β and energy. The array of bars at the top represents θ^β listed in Table I. (c) The lower part of (a), where the first-order gaps of the single moiré pattern $\lambda = \alpha$ and β are highlighted by red and blue curves, respectively, and higher-order gaps are marked by green curves. (b) The corresponding map of the energy gaps with the vertical axis converted to the electron density, where the size of the black dots represents the gap width.
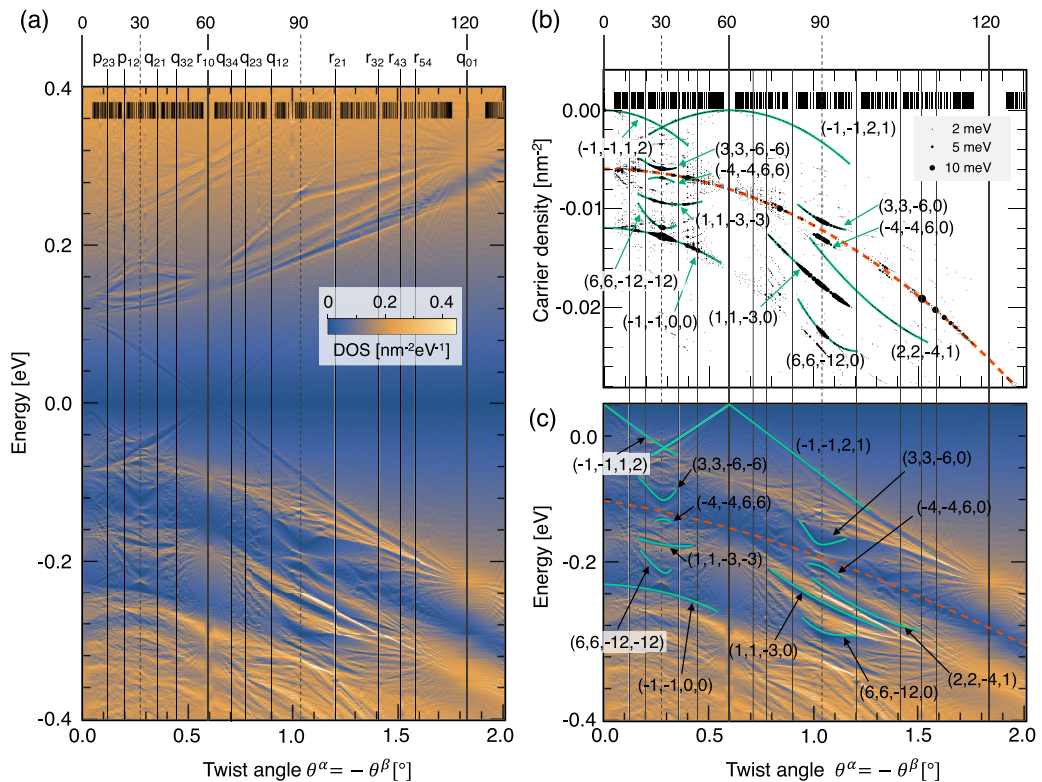
FIG. 7. Plots similar to Fig. 6 for series II $[(\theta^\alpha, \theta^\beta) = (\theta, -\theta)]$. The vertical lines labeled by p_{mn}, q_{mn}, r_{mn} represent the commensurate angles defined in Eq. (10), and the numbers at the top $(0, 30, \ldots, 120)$ indicate the relative angle between the two moiré patterns, $\phi^\beta - \phi^\alpha$.

terms which combine the reciprocal vectors of the different moiré patterns. We can also define two more unit areas,

$$A_5 = \left(\mathbf{G}_2^\alpha \times \mathbf{G}_1^\beta\right)_z, \quad A_6 = \left(\mathbf{G}_2^\alpha \times \mathbf{G}_2^\beta\right)_z, \quad (20)$$

which are shown as dashed parallelograms in Fig. 2. In the hBN/graphene/hBN system, however, they are not independent and can be expressed as $A_5 = -A_3 - A_4$ and $A_6 = A_3$, considering that the angle between $\mathbf{G}_1^\lambda$ and $\mathbf{G}_2^\lambda$ is fixed to $120°$. Therefore, a complete set of independent unit areas is given by (A_1, A_2, A_3, A_4). The areas $A_1, \ldots, A_6$ can be regarded as the projection of the faces of a four-dimensional hypercube onto the physical 2D plane, which is analogous to the general argument of a quasicrystal [55].

In a conventional periodic 2D system with primitive reciprocal lattice vectors $\mathbf{G}_1$ and $\mathbf{G}_2$, the electronic spectrum is separated into Bloch subbands, each of which accommodates the electron density $|\mathbf{G}_1 \times \mathbf{G}_2|/(2\pi)^2$. In a doubly periodic 2D system, in contrast, the areas $A_1, \ldots, A_4$ all serve as units of the spectrum separation. More specifically, we find that the electron density (per spin and valley) from the Dirac point to any gap in the hBN/graphene/hBN system can be uniquely expressed by four integers, m_1, m_2, m_3, m_4, as

$$n_e = (m_1 A_1 + m_2 A_2 + m_3 A_3 + m_4 A_4)/(2\pi)^2. \quad (21)$$

These integers never change as long as the gap survives in a continuous change of the moiré pattern.

Figure 6(c) shows m_1, m_2, m_3, m_4 found for some major gaps in case I. Figure 6(b) is the same plot, but with the vertical axis being the electron density n_e, and the black dots represent spectral gaps, with the size indicating gap width. Here the integers $m_1, \ldots, m_4$ are identified from the commensurate approximants as follows. In a commensurate case, A_1, A_2, A_3, and A_4 have the greatest common divisor $A_{SM} = (\mathbf{G}_1^{SM} \times \mathbf{G}_2^{SM})_z$ (the area of the first Brillouin zone for the supermoiré period), so they can be written as $A_i = s_i A_{SM}$ with integers s_i ($i = 1, 2, 3, 4$). n_e is also quantized in units of $A_{SM}/(2\pi)^2$, and each band gap is characterized by an integer $t = n_e/[A_{SM}/(2\pi)^2]$, which is the number of occupied subbands measured from the Dirac point. Then Eq. (21) becomes the Diophantine equation $t = m_1 s_1 + m_2 s_2 + m_3 s_3 + m_4 s_4$. For each gap in Fig. 6(c), we have as many Diophantine equations as the number of the data points (i.e., the different systems), and (m_1, m_2, m_3, m_4) is obtained as a unique solution of the set of equations. Here note that the area $m_1 A_1 + m_2 A_2 + m_3 A_3 + m_4 A_4$ is a continuous function of the twist angle, while A_{SM} (and thus t, s_i) can be defined only for commensurate systems and it discontinuously changes with changing the twist angle. This result indicates that the same (m_1, m_2, m_3, m_4) are shared by infinitely many commensurate approximants (with A_{SM} ranging from zero to infinity) which exist in close vicinity to a specific $(\theta^\alpha, \theta^\beta)$, and hence, it is valid in the limit of $A_{SM} \to \infty$, i.e., incommensurate systems.

Figures 7(b) and 7(c) are similar plots for case II. Here the condition $|\theta^\alpha| = |\theta^\beta|$ forces $A_1 = A_2$, and then m_1 and m_2 become indeterminate. We can resolve the two integers by considering an infinitesimal rotation of either the top or bottom hBN layer, and it turns out that $m_1 = m_2$ for any gaps in case II. This is explicitly proved as fol-

lows. By starting from a case-II system $(\theta^\alpha, \theta^\beta) = (\theta, -\theta)$, we can consider two distinct systems, $X : (\theta^\alpha, \theta^\beta) = (\theta + \delta\theta, -\theta)$ and $X' : (\theta^\alpha, \theta^\beta) = (\theta, -\theta - \delta\theta)$. Systems X and X' are actually identical if we turn the whole system $180°$ with respect to an in-plane axis, and hence, they have exactly the same energy spectrum. The same energy gap is labeled by a different set of integers as m_i and m_i' for X and X', respectively, which satisfy $\sum_i m_i A_i = \sum_i m_i' A_i'$. Considering that the layers $\lambda = \alpha, \beta$ are interchanged in the $180°$-rotation process, the unit areas of X and X' are related by $(A_1, A_2, A_3, A_4) = (A_2', A_1', A_3', A_4')$, which leads to the condition $(m_1, m_2, m_3, m_4) = (m_2', m_1', m_3', m_4')$. When the gap survives in the limit of $\delta\theta \to 0$, we have $m_i = m_i'$, and hence, we conclude $m_1 = m_2$. The constraint $m_1 = m_2$ explains why the first-order gap of the individual moiré potential, $(\pm 1, 0, 0, 0)$ and $(0, \pm 1, 0, 0)$, cannot open in Fig. 7(b).

Figures 6 and 7 also include $(\theta^\alpha, \theta^\beta) = (0°, 0°)$, where the two hBNs have the exact same periodicity. At $(0°, 0°)$, the spectrum has a series of the Bloch gaps of a single moiré pattern, where the electronic density n_e is quantized into integer multiples of $A_1/(2\pi) = A_2/(2\pi)$. In Figs. 6 and 7, however, most of these gaps are smeared in averaging over Δr_0, leaving only the $(0,0,0,0)$ gap at the Dirac point. This result also agrees with the above statement that gaps of $(m, 0, 0, 0)$ and $(0, m, 0, 0)$ with nonzero m are not allowed (cannot be a continuous region on changing the twist angle) for $(\theta^\alpha, \theta^\beta) = (\theta, -\theta)$.

The constraint among the six unit areas $A_1, \ldots, A_6$ can be broken by uniformly distorting either the top or bottom hBN layer such that $120°$ symmetry is broken. If we extend the parameter space to such distorted systems, we should need six integers $(m_1, \cdots, m_6)$ to characterize minigaps, where the electron density is given by $\sum_{i=1}^6 m_i A_i$. This is similar to the situation in series II, where m_1 and m_2 can be resolved by breaking the condition $A_1 = A_2$.

C. Quasi-Brillouin zones

Actually, the area $m_1 A_1 + m_2 A_2 + m_3 A_3 + m_4 A_4$ can be associated with a specific region in momentum space, which is referred to as the quasi-Brillouin zone. In a conventional periodic 2D system defined by $\mathbf{G}_1$ and $\mathbf{G}_2$, the Brillouin zones ($n = 1, 2, 3, \ldots$) are defined by a series of certain regions bounded by the Bragg planes, i.e., the perpendicular bisectors of the reciprocal vectors $n_1 \mathbf{G}_1 + n_2 \mathbf{G}_2$ [56]. There all the Brillouin zones have an equal area of $|\mathbf{G}_1 \times \mathbf{G}_2|$, and therefore, the carrier density below any gap is quantized to an integer multiple of the area. In a doubly periodic 2D system, similarly, we can define a quasi-Brillouin zone as an area bound by the Bragg planes for composite reciprocal vectors $p\mathbf{G}_1^\alpha + q\mathbf{G}_2^\alpha + r\mathbf{G}_1^\beta + s\mathbf{G}_2^\beta$. In conventional three-dimensional quasicrystals such as Al-Mn alloys, the idea of the quasi-Brillouin zones was used to explain the pseudogaps and the stability of the system [57]. In an incommensurate case, generally, momentum space is filled by infinitely many Bragg planes, and there is no systematic way to define quasi-Brillouin zones as in the periodic case. But here we claim that each single gap in the spectrum can be associated with a specific figure, and the area is equal to $m_1 A_1 + m_2 A_2 + m_3 A_3 + m_4 A_4$. Such
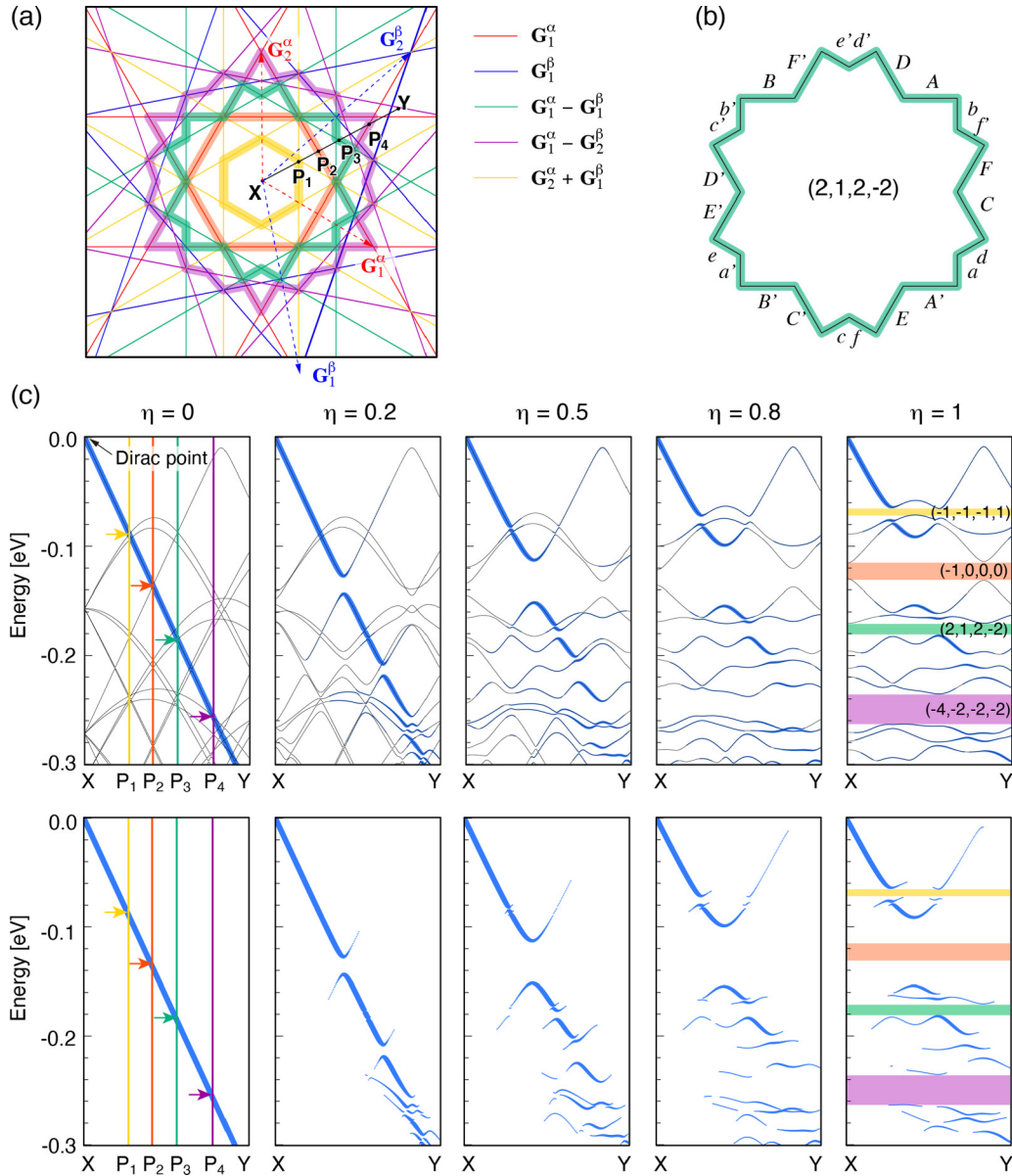
FIG. 8. (a) Quasi-Brillouin zones of $(\theta^\alpha, \theta^\beta) = (0°, 1.1908°)$, where thick lines in different colors correspond to the four gaps indicated in (c). Thin lines are the Bragg planes corresponding to different reciprocal lattice vectors. For instance, the red lines are the perpendicular bisector of $\mathbf{G}_1^\alpha$ and its $60n°$ rotation. (b) Quasi-Brillouin zone of the gap $(2, 1, 2, -2)$, where x and x' represent a pair of boundary segments connected by the moiré potential. (c) Band structure on a path from X to Y shown in (a) calculated for $(0°, 1.1908°)$ with the moiré potentials reduced by the factor η $(0 \leqslant \eta \leqslant 1)$. The black solid lines represent the band dispersion plotted in the extended zone scheme, and the blue dots represent the spectral weight $A(\mathbf{q}, \varepsilon)$. The bottom panels show the same plot without the band lines.

figures include a simple hexagon defined by a single reciprocal vector as considered in previous works [25,27,28], but more generally, they can be a nonconvex polygon composed of multiple segments of different Bragg planes, as shown in Fig. 8(a).

The shape of the quasi-Brillouin zone for a given gap can be specified by the plain wave projection with the zero-potential limit as follows. Let us explain the scheme using a simple 1D Hamiltonian with a single periodic potential, $H = -\partial^2/\partial x^2 + 2V_0 \cos Gx$, where $G = 2\pi$. The eigenenergy and the eigenfunctions are labeled as ε_{nk} and $|\psi_{nk}\rangle$, respectively, where n is the band index and k is the Bloch wave number in the first Brillouin zone $(-\pi \leqslant k \leqslant \pi)$. Figure 9 shows

the band structures calculated for different potential amplitudes, $V_0 = 0, 5, 10$. The black solid lines represent the band dispersion ε_{nk} plotted in the extended zone scheme, and the size of overlapping blue points represents the spectral weight projected to the plain wave, or

$$A(q, \varepsilon) = \sum_{n,k} |\langle q|\psi_{nk}\rangle|^2 \delta(\varepsilon - \varepsilon_{nk}), \qquad (22)$$

where $|q\rangle = e^{iqx}$ is the plain wave, with $-\infty < q < \infty$, and the summation in k is taken over the first Brillouin zone. The pink regions indicate the first and second energy gaps. With decreasing potential amplitude V_0, the gaps narrow, and the spectral weight approaches a simple parabola, $\varepsilon = q^2$. In the
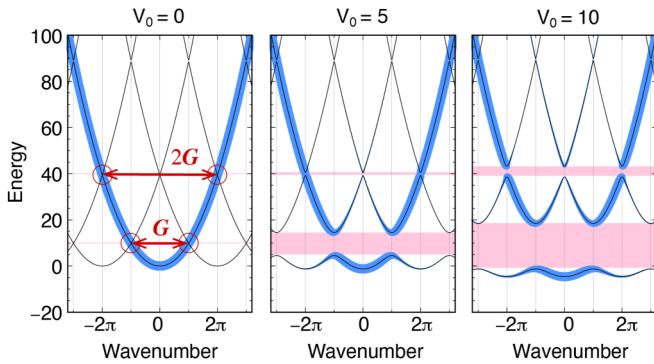
FIG. 9. Band structure of a 1D Hamiltonian $H = -\partial^2/\partial x^2 + 2V_0 \cos Gx$, with $V_0 = 0, 5, 10$. The black solid lines represent the band dispersion ε_{nk} in the extended zone scheme, and the size of the blue points represents the spectral weight projected to the plain wave $A(q, \varepsilon)$.

limit of $V_0 \to 0$, we can specify the points on the parabola at which the energy gap opens in an infinitesimal V_0 (marked by red circles). These points actually determine the Brillouin zone boundary.

The same strategy works for the double period system as well. In our hBN/graphene/hBN system, we define the spectral weight as

$$A(\mathbf{q}, \varepsilon) = \sum_{\alpha} \sum_{X} |\langle \mathbf{q}, X | \psi_\alpha \rangle|^2 \delta(\varepsilon - \varepsilon_\alpha), \quad (23)$$

where ε_α and $|\psi_\alpha\rangle$ are the eigenenergy and the eigenstates of the system and $|\mathbf{q}, X\rangle$ is the plain wave basis of the sublattice $X = A, B$ of the monolayer graphene. For example, we take the commensurate approximant for $(\theta^\alpha, \theta^\beta) = (0°, 1.1908°)$ considered in Figs. 4 and 5 and calculate the eigenstates of the Hamiltonian (11) with the moiré potentials $(V_{hBN}^\alpha, V_{hBN}^\beta)$ reduced by the factor η ($0 \leqslant \eta \leqslant 1$). Figure 8(c) shows the band structures from $\eta = 0$ to 1, calculated on a path from X (graphene's Dirac point) to a certain point Y, shown in Fig. 8(a). The black solid lines represent the band dispersion plotted in the extended zone scheme, and the blue dots represent the spectral weight $A(\mathbf{q}, \varepsilon)$. At $\eta = 0$, we just have graphene's Dirac cone. By tracing the gaps in the spectral weight while decreasing η from 1 to 0, we can specify the gap opening points just as in the 1D case.

In Fig. 8(c), we consider four gaps with different indexes of $(m_1, ..., m_4)$. Here $(-1, 0, 0, 0)$ is the first-order gap of the moiré potential $\lambda = \alpha$, and others are double moiré gaps caused by the coexistence of the two moiré patterns. In the limit $\eta \to 0$, we find the gap-opening wave numbers $P_1, \ldots, P_4$ for these gaps. By following the same procedure for paths in different directions, we finally obtain the quasi-Brillouin zone on the (k_x, k_y) plane as the traces of $P_1, \ldots, P_4$, which are illustrated as thick colored lines in Fig. 8(a). The quasi Brillouin zone is composed of segments of the Bragg planes, which are shown as thin lines. The first-order gap $(-1, 0, 0, 0)$ gives a regular hexagon, which is the first Brillouin zone of the moiré potential of $\lambda = \alpha$. The double moiré gap $(-1, -1, -1, 1)$ also gives a hexagon, but with a smaller size, which corresponds to the first Brillouin zone of small reciprocal lattice vectors $\mathbf{G}_2^\alpha + \mathbf{G}_1^\beta$. In contrast, the

gaps $(2, 1, 2, -2)$ and $(-4, -2, -2, -2)$ are associated with flowerlike complex polygons composed of multiple Bragg line segments. In each case, the area of the polygon is shown to be exactly equal to $m_1 A_1 + m_2 A_2 + m_3 A_3 + m_4 A_4$. Just like the conventional Brillouin zone in a periodic system, the quasi-Brillouin zone is also a closed object in that any sides of the boundary are precisely stuck to the other side, and one can never go out of the region by crossing the boundary.

The quasi-Brillouin zone continuously changes when changing the twist angle, regardless of the unit cell size of the commensurate approximants. Figure 10 shows the same plot calculated for a slightly different angle, $(\theta^\alpha, \theta^\beta) = (0, 1.2967°)$ [labeled (iii) in Fig. 6]. The supermoiré unit area of the system is about 10 times greater than that of Fig. 8(c), and accordingly, we see many more band lines due to the band folding into the smaller Brillouin zone. If we see the spectral weight (blue dots), however, we find that it exhibits a structure similar to Fig. 8(c) [except that the gap $(-1, -1, -1, 1)$ is not fully open], and the gaps close at the Bragg planes with the same indexes in the limit of $\eta \to 0$. As a result, we end up with nearly the same shape for the quasi-Brillouin zone as shown in Fig. 11, plot (iii). In Fig. 10, we see a number of extra band lines just overlap but hardly contribute to the spectral weight, and therefore. they are neglected in the identification of the zone boundary. Because of this, the quasi-Brillouin zone obtained here is generally different from one obtained by sorting all the eigenvalues in energy and tracking the same level index in the limit of the zero potential [58], which is fully affected by all the overlapping band lines.

In Fig. 11, we show the continuous evolution of the quasi-Brillouin zones as a function of the twist angle from plot (i) to plot (v) (corresponding to the labels in Fig. 6), where the shape continuously changes regardless of the discontinuous change of the rigorous period of the approximants. The area of the quasi Brillouin zone is always equal to $m_1 A_1 + m_2 A_2 + m_3 A_3 + m_4 A_4$.

Last, we comment on connections of the integers m_i to the topological properties. We have several analogous situations in which the electron density is quantized by topological numbers. In a singly periodic system (the usual Bloch system), the electron density is quantized as $n_e = mA/(2\pi)^d$, where A is the unit volume of the d-dimensional Brillouin zone and the integer m (the number of bands) is a zero-dimensional topological number, just as mentioned in Sec. I. For double period systems, we have an analogous situation in a 1D system $H = p^2/(2m) + V_\alpha(x) + V_\beta(x)$, where V_α and V_β are periodic potentials with wave numbers G_α and G_β, respectively. The electron density below each gap is given by $n_e = (m_\alpha G_\alpha + m_\beta G_\beta)/(2\pi)$ with integers m_α and m_β. At the same time, m_α and m_β are also related to the adiabatic charge pumping [41–44], where m_λ ($\lambda = \alpha, \beta$) represents the number of pumped electrons under an adiabatic translation of V_λ by a single period. When the ratio G_α/G_β is rational (i.e., the two periods are commensurate), in particular, m_α and m_β are expressed as Chern numbers. For irrational systems, the Chern number cannot be defined, while a very recent work proposed a mathematical scheme to topologically characterize the charge pumping in 1D quasiperiodic systems [59]. The present system, where the electron density is given by
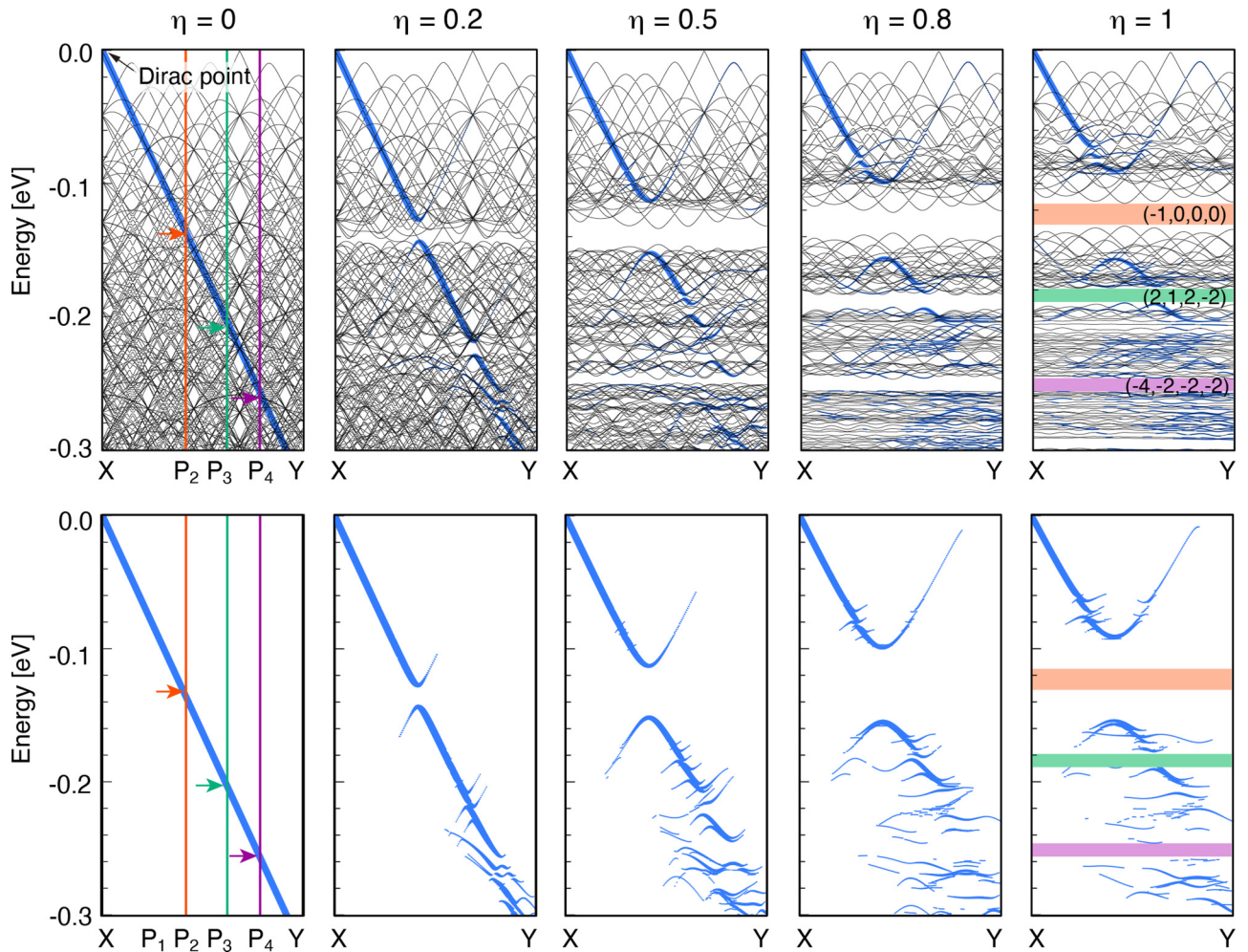
FIG. 10. Plot similar to Fig. 8(c) calculated for $(\theta^\alpha, \theta^\beta) = (0°, 1.2967°)$.

$n_e = \sum_i m_i A_i/(2\pi)^2$, is a natural extension of the problem to two dimensions, and it strongly implies that integers $m_1, \ldots, m_4$ are also related to the charge pumping in two dimensions. Actually, the 2D adiabatic pumping in the commensurate case is shown to be characterized by sliding Chern numbers [44,60,61], and we expect that $m_1, \ldots, m_4$ should be related to these numbers, while we leave verifying these relationships for future works. Further studies on this problem

would shed light on a hidden relationship between quasicrystal and topological physics.

IV. CONCLUSION

We theoretically studied the electronic structure of the hBN/graphene/hBN double moiré system as a function of the top and bottom twist angles and demonstrated that the
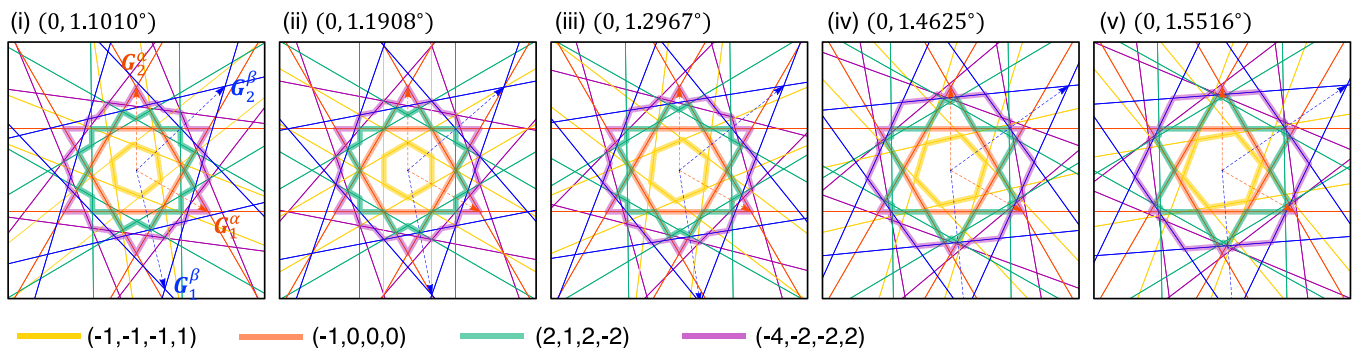
FIG. 11. Quasi-Brillouin zones similar to Fig. 8(a) calculated for five different angles. The indexes (i) to (v) correspond to the labels in Fig. 6.

spectrum consists of a number of fractal minigaps. Specifically, each energy gap is characterized by a set of integers $(m_1, \ldots, m_4)$, where the electron density below the gap is given by $n_e = \sum_i m_i A_i / (2\pi)^2$ with characteristic momentum space areas $A_1, \ldots, A_4$. The area $\sum_i m_i A_i$ corresponds to a quasi-Brillouin zone bounded by multiple Bragg planes, which can be uniquely identified by the spectral distribution in the zero-potential limit. In changing the twist angles, the quasi-Brillouin zone also changes continuously regardless of the commensurability of the double moiré pattern.

We neglected the lattice relaxation effect throughout this work for simplicity, while the general theoretical scheme to characterize the band gap is valid as long as the system has a well-defined double period. The band-gap characterization proposed in this work should also be useful in other quasiperiodic 2D systems, such as twisted trilayer graphene [34–37],

twisted bilayer graphene on hBN [31–33], and 30° twisted bilayer graphene [46–49].

APPENDIX: LIST OF COMMENSURATE APPROXIMANTS

We present the list of approximate commensurate systems in series I in Table I, and those in series II in Table II. Tables I and II show the twist angle, a set of integers $(n_1^\alpha, n_2^\alpha, n_1^\beta, n_2^\beta)$, the supermoiré period L^{SM}, and the correction ΔL from the original incommensurate structure.

TABLE I. List of approximate commensurate systems of series I, $(\theta^\alpha, \theta^\beta) = (0, \theta)$. L^{SM} (nm) is the supermoiré period, and ΔL (nm) is the correction from the original incommensurate structure (see the text).

| θ (deg)	n_1^α	n_2^α	n_1^β	n_2^β	L^{SM}	ΔL	θ (deg)	n_1^α	n_2^α	n_1^β	n_2^β	L^{SM}	ΔL	θ (deg)	n_1^α	n_2^α	n_1^β	n_2^β	L^{SM}	ΔL
0.0000	1	0	1	0	13.92	0	0.6946	6	6	−1	13	144.64	0.4885	1.2855	10	9	−10	30	229.12	0.1110
0.0992	6	6	5	7	144.64	0.0120	0.6985	11	1	6	10	160.51	0.4494	1.2967	5	1	0	9	77.49	0.0913
0.1083	11	11	9	13	265.18	0.0262	0.7009	11	6	2	17	207.84	0.3282	1.3109	8	7	−8	24	180.94	0.3575
0.1191	5	5	4	6	120.54	0.0144	0.7145	5	0	3	4	69.59	0.2464	1.3152	9	1	1	15	132.77	0.2972
0.1323	9	9	7	11	216.97	0.0319	0.7320	4	9	−5	16	160.51	0.1011	1.3238	3	10	−14	22	164.09	0.0440
0.1489	4	4	3	5	96.43	0.0179	0.7372	12	5	3	17	210.62	0.3335	1.3296	7	10	−13	28	205.97	0.1582
0.1624	11	0	10	2	153.10	0.0337	0.7443	4	4	−1	9	96.43	0.3654	1.3477	6	9	−12	25	182.01	0.2393
0.1701	7	7	5	9	168.75	0.0408	0.7513	7	12	−6	23	231.65	0.1193	1.3480	10	9	−11	31	229.12	0.3407
0.1786	10	0	9	2	139.18	0.0370	0.7550	11	4	3	15	187.25	0.3104	1.3526	10	5	−5	24	184.12	0.1326
0.1985	3	3	2	4	72.32	0.0237	0.7655	7	0	4	6	97.43	0.3867	1.3599	10	1	1	17	146.64	0.1881
0.2137	11	3	9	6	177.70	0.4663	0.7775	3	10	−7	17	164.09	0.1983	1.3666	9	8	−10	28	205.03	0.2428
0.2165	11	11	7	15	265.18	0.1029	0.7822	9	7	−1	18	193.36	0.3986	1.3831	2	10	−15	21	154.99	0.0052
0.2233	8	0	7	2	111.35	0.0459	0.7852	12	10	−2	25	265.54	0.0584	1.3900	8	7	−9	25	180.94	0.1668
0.2382	5	5	3	7	120.54	0.0563	0.7939	3	3	−1	7	72.32	0.3046	1.4086	2	6	−9	14	100.37	0.1440
0.2457	12	5	9	9	210.62	0.3425	0.8042	11	9	−2	23	241.47	0.0927	1.4207	7	6	−8	22	156.85	0.1219
0.2481	12	12	7	17	289.29	0.1464	0.8087	8	6	−1	16	169.32	0.1624	1.4356	4	8	−12	21	147.30	0.0359
0.2552	7	0	6	2	97.43	0.0521	0.8203	5	3	0	9	97.43	0.3427	1.4492	6	10	−15	28	194.86	0.2768
0.2646	9	9	5	13	216.97	0.1245	0.8273	10	8	−2	21	217.41	0.2860	1.4571	10	8	−11	31	217.41	0.3157
0.2707	11	11	6	16	265.18	0.1589	0.8344	12	8	−1	23	242.67	0.1292	1.4625	6	5	−7	19	132.77	0.1229
0.2977	2	2	1	3	48.21	0.0347	0.8440	7	5	−1	14	145.31	0.1614	1.4716	10	3	−3	22	164.09	0.0317
0.3248	11	0	9	4	153.10	0.1302	0.8518	9	5	0	16	171.03	0.0635	1.4904	9	7	−10	28	193.36	0.2114
0.3308	9	9	4	14	216.97	0.1911	0.8577	11	5	1	18	197.33	0.1873	1.5103	3	8	−13	20	137.08	0.1014
0.3402	7	7	3	11	168.75	0.1568	0.8606	11	7	−1	21	218.74	0.3712	1.5228	5	4	−6	16	108.71	0.1957
0.3450	12	7	7	13	231.65	0.1751	0.8931	2	0	1	2	27.84	0.1415	1.5330	8	6	−9	25	169.32	0.0362
0.3573	5	0	4	2	69.59	0.0709	0.9287	5	11	−9	22	197.33	0.0240	1.5516	3	2	−3	9	60.67	0.1985
0.3721	8	8	3	13	192.86	0.2124	0.9346	5	9	−7	19	171.03	0.0970	1.5689	4	10	−17	26	173.84	0.1515
0.3789	11	11	4	18	265.18	0.3021	0.9423	5	7	−5	16	145.31	0.3127	1.5785	1	8	−14	17	118.92	0.0345
0.3970	3	3	1	5	72.32	0.0899	0.9498	3	7	−6	14	123.71	0.4554	1.5898	7	5	−8	22	145.31	0.2386
0.4168	10	10	3	17	241.07	0.3281	0.9519	8	12	−9	27	242.67	0.1934	1.5999	1	9	−16	19	132.77	0.3700
0.4253	7	7	2	12	168.75	0.2385	0.9662	3	5	−4	11	97.43	0.1633	1.6065	8	5	−8	24	158.08	0.1204
0.4303	11	7	5	14	218.74	0.0922	0.9777	6	8	−6	19	169.32	0.1629	1.6173	4	3	−5	13	84.66	0.3899
0.4466	4	0	3	2	55.67	0.0861	0.9829	12	5	0	21	210.62	0.0849	1.6210	9	5	−8	26	171.03	0.3885
0.4631	9	9	2	16	216.97	0.3587	0.9923	3	3	−2	8	72.32	0.4324	1.6281	2	10	−18	23	154.99	0.1456
0.4673	5	9	−1	14	171.03	0.2277	1.0043	7	9	−7	22	193.36	0.1051	1.6406	5	3	−5	15	97.43	0.1220
0.4763	5	5	1	9	120.54	0.2098	1.0108	4	6	−5	14	121.34	0.3894	1.6590	6	3	−5	17	110.47	0.0304
0.4872	11	0	8	6	153.10	0.2776	1.0250	8	10	−8	25	217.41	0.1063	1.6735	7	3	−5	19	123.71	0.1045
0.4962	6	6	1	11	144.64	0.2711	1.0314	8	3	0	14	137.08	0.1263	1.6853	8	3	−5	21	137.08	0.1239
0.5104	7	0	5	4	97.43	0.1921	1.0524	1	8	−9	14	118.92	0.3587	1.6950	9	3	−5	23	150.55	0.1037
0.5210	8	8	1	15	192.86	0.3947	1.0909	8	10	−9	26	217.41	0.3308	1.7030	10	3	−5	25	164.09	0.0541

TABLE I. *(Continued.)*

θ (deg)	n_1^α	n_2^α	n_1^β	n_2^β	L^{SM}	ΔL	θ (deg)	n_1^α	n_2^α	n_1^β	n_2^β	L^{SM}	ΔL	θ (deg)	n_1^α	n_2^α	n_1^β	n_2^β	L^{SM}	ΔL
0.5262	1	8	−4	11	118.92	0.4765	1.1010	1	6	−7	11	91.27	0.0852	1.7861	1	0	0	2	13.92	0.1866
0.5293	9	9	1	17	216.97	0.4567	1.1126	9	6	−4	21	182.01	0.2095	1.8700	3	10	−21	27	164.09	0.3471
0.5359	10	0	7	6	139.18	0.2995	1.1199	2	7	−8	14	113.93	0.3313	1.8732	2	10	−21	25	154.99	0.1910
0.5391	12	9	3	19	253.99	0.4594	1.1381	2	10	−12	19	154.99	0.2998	1.8781	3	9	−19	25	150.55	0.3026
0.5440	1	11	−6	15	160.51	0.1779	1.1485	5	10	−11	23	184.12	0.3826	1.8822	2	9	−19	23	141.26	0.2703
0.5954	1	1	0	2	24.11	0.0625	1.1908	1	1	−1	3	24.11	0.1884	1.8878	3	8	−17	23	137.08	0.2860
0.6429	12	1	7	10	174.40	0.0461	1.2305	10	6	−5	24	194.86	0.3106	1.8932	2	8	−17	21	127.56	0.3269
0.6495	11	0	7	8	153.10	0.4613	1.2364	9	5	−4	21	171.03	0.3948	1.8995	3	7	−15	21	123.71	0.3057
0.6518	9	12	−3	23	253.99	0.1949	1.2402	10	3	−1	19	164.09	0.2320	1.9069	2	7	−15	19	113.93	0.3527
0.6576	9	1	5	8	132.77	0.2049	1.2487	9	2	0	16	141.26	0.3119	1.9140	3	6	−13	19	110.47	0.3742
0.6698	8	0	5	6	111.35	0.3536	1.2713	6	2	−1	12	100.37	0.3496	1.9243	2	6	−13	17	100.37	0.3359
0.6900	12	7	2	19	231.65	0.0804	1.2809	5	8	−10	21	158.08	0.2224	1.9345	10	3	−7	28	164.09	0.0546

TABLE II. List of approximate commensurate systems of series II, $(\theta^\alpha, \theta^\beta) = (\theta, -\theta)$. L^{SM} (nm) is the supermoiré period, and ΔL (nm) is the correction from the original incommensurate structure.

θ (deg)	n_1^α	n_2^α	n_1^β	n_2^β	L^{SM}	ΔL	θ (deg)	n_1^α	n_2^α	n_1^β	n_2^β	L^{SM}	ΔL	θ (deg)	n_1^α	n_2^α	n_1^β	n_2^β	L^{SM}	ΔL
0.0000	1	0	1	0	13.92	0	0.3082	12	5	17	−5	201.65	0	0.5656	13	12	25	−12	263.73	0
0.0496	11	13	13	11	289.28	0	0.3155	7	3	10	−3	118.21	0	0.5668	13	13	26	−12	274.07	0.2702
0.0541	5	6	6	5	132.59	0	0.3209	3	10	10	3	156.56	0	0.5679	14	13	27	−13	284.55	0
0.0576	15	1	16	−1	215.73	0	0.3230	12	14	23	−1	299.13	0.2946	0.5690	15	13	28	−14	295.14	0.2507
0.0595	9	11	11	9	241.07	0	0.3251	9	4	13	−4	152.96	0	0.5699	15	14	29	−14	305.36	0
0.0616	14	1	15	−1	201.81	0	0.3311	2	7	7	2	108.38	0	0.5972	1	0	1	−1	12.02	0
0.0662	4	5	5	4	108.48	0	0.3339	15	13	26	−4	321.09	0.2727	0.6252	14	15	29	−15	298.26	0
0.0715	12	1	13	−1	173.97	0	0.3353	13	6	19	−6	222.48	0	0.6262	14	14	28	−15	287.79	0.2446
0.0744	7	9	9	7	192.85	0	0.3383	15	7	22	−7	257.24	0	0.6273	13	14	27	−14	277.44	0
0.0777	11	1	12	−1	160.05	0	0.3406	3	11	11	3	168.59	0	0.6285	12	14	26	−13	267.23	0.2632
0.0851	3	4	4	3	84.37	0	0.3451	4	15	15	4	228.79	0	0.6297	12	13	25	−13	256.63	0
0.0916	11	15	15	11	313.37	0	0.3577	2	1	3	−1	34.76	0	0.6311	12	12	24	−13	246.15	0.2847
0.0940	9	1	10	−1	132.21	0	0.3726	3	13	13	3	192.63	0	0.6326	11	12	23	−12	235.81	0
0.0992	5	7	7	5	144.63	0	0.3765	15	8	23	−8	264.13	0	0.6360	10	11	21	−11	215.00	0
0.1051	8	1	9	−1	118.29	0	0.3794	2	9	9	2	132.43	0	0.6402	9	10	19	−10	194.18	0
0.1083	9	13	13	9	265.15	0	0.3817	13	15	26	−4	316.44	0.2687	0.6453	8	9	17	−9	173.37	0
0.1117	15	2	17	−2	222.67	0	0.3833	11	6	17	−6	194.61	0	0.6519	7	8	15	−8	152.55	0
0.1191	2	3	3	2	60.26	0	0.3858	3	14	14	3	204.65	0	0.6559	13	15	28	−15	284.29	0
0.1276	13	2	15	−2	194.83	0	0.3888	9	5	14	−5	159.86	0	0.6606	6	7	13	−7	131.74	0
0.1295	9	14	14	9	277.19	0	0.3975	1	5	5	1	72.23	0	0.6660	11	13	24	−13	242.66	0
0.1323	7	11	11	7	216.93	0	0.4024	13	12	24	−6	280.47	0.2992	0.6724	5	6	11	−6	110.92	0
0.1374	6	1	7	−1	90.45	0	0.4039	12	7	19	−7	215.44	0	0.6775	15	1	15	−16	180.10	0
0.1407	14	14	20	7	334.35	0.2842	0.4128	5	3	8	−3	90.34	0	0.6802	9	11	20	−11	201.03	0
0.1418	8	13	13	8	253.08	0	0.4209	13	8	21	−8	236.26	0	0.6832	14	1	14	−15	168.09	0
0.1489	3	5	5	3	96.41	0	0.4222	14	14	27	−7	311.94	0.2651	0.6898	4	5	9	−5	90.11	0
0.1567	7	12	12	7	228.97	0	0.4260	1	6	6	1	84.25	0	0.6976	12	1	12	−13	144.05	0
0.1624	5	1	6	−1	76.53	0	0.4302	12	13	24	−6	277.82	0.2963	0.7019	7	9	16	−9	159.40	0
0.1702	5	9	9	5	168.71	0	0.4319	11	7	18	−7	201.50	0	0.7067	11	1	11	−12	132.03	0
0.1729	14	3	17	−3	215.68	0	0.4352	14	9	23	−9	257.08	0	0.7177	3	4	7	−4	69.29	0
0.1752	6	11	11	6	204.86	0	0.4374	2	13	13	2	180.51	0	0.7274	11	15	26	−15	256.34	0
0.1766	15	13	22	4	332.86	0.2827	0.4473	3	2	5	−2	55.58	0	0.7311	9	1	9	−10	107.99	0
0.1787	9	2	11	−2	139.15	0	0.4561	2	15	15	2	204.55	0	0.7390	5	7	12	−7	117.76	0
0.1813	8	15	15	8	277.16	0	0.4602	13	9	22	−9	243.14	0	0.7478	8	1	8	−9	95.97	0
0.1848	13	3	16	−3	201.76	0	0.4640	1	8	8	1	108.29	0	0.7527	9	13	22	−13	214.70	0
0.1985	1	2	2	1	36.15	0	0.4710	7	5	12	−5	131.98	0	0.7579	15	2	15	−17	179.93	0
0.2102	15	4	19	−4	236.52	0	0.4773	1	9	9	1	120.30	0	0.7694	2	3	5	−3	48.47	0
0.2144	11	3	14	−3	173.91	0	0.4802	15	11	26	−11	284.77	0	0.7827	13	2	13	−15	155.89	0

TABLE II. *(Continued.)*.

θ (deg)	n_1^α	n_2^α	n_1^β	n_2^β	L^{SM}	ΔL	θ (deg)	n_1^α	n_2^α	n_1^β	n_2^β	L^{SM}	ΔL	θ (deg)	n_1^α	n_2^α	n_1^β	n_2^β	L^{SM}	ΔL
0.2166	7	15	15	7	265.07	0	0.4882	4	3	7	−3	76.40	0	0.7856	9	14	23	−14	221.54	0
0.2195	6	13	13	6	228.93	0	0.4972	1	11	11	1	144.34	0	0.7902	7	11	18	−11	173.06	0
0.2207	13	15	22	4	330.18	0.2804	0.5012	9	7	16	−7	173.61	0	0.7924	13	12	24	−18	238.22	0.2541
0.2234	7	2	9	−2	111.30	0	0.5049	1	12	12	1	156.36	0	0.7982	6	1	6	−7	71.93	0
0.2291	4	9	9	4	156.63	0	0.5115	5	4	9	−4	97.21	0	0.8034	14	14	27	−20	265.35	0.2255
0.2331	10	3	13	−3	159.99	0	0.5172	1	14	14	1	180.40	0	0.8052	8	13	21	−13	200.71	0
0.2383	3	7	7	3	120.48	0	0.5198	11	9	20	−9	215.24	0	0.8166	3	5	8	−5	76.12	0
0.2453	5	12	12	5	204.81	0	0.5222	1	15	15	1	192.41	0	0.8293	7	12	19	−12	179.89	0
0.2553	3	1	4	−1	48.69	0	0.5266	6	5	11	−5	118.03	0	0.8315	12	13	24	−18	233.83	0.2494
0.2648	5	13	13	5	216.84	0	0.5323	13	11	24	−11	256.87	0	0.8386	5	1	5	−6	59.91	0
0.2708	3	8	8	3	132.51	0	0.5372	7	6	13	−6	138.84	0	0.8514	5	9	14	−9	131.42	0
0.2733	14	12	23	−1	303.06	0.2984	0.5414	15	13	28	−13	298.50	0	0.8559	14	3	14	−17	167.71	0
0.2750	11	4	15	−4	180.82	0	0.5450	8	7	15	−7	159.66	0	0.8597	6	11	17	−11	159.07	0
0.2765	0	26	15	15	349.32	0.2585	0.5511	9	8	17	−8	180.47	0	0.8620	15	13	26	−22	258.22	0.2193
0.2781	4	11	11	4	180.69	0	0.5558	10	9	19	−9	201.29	0	0.8656	9	2	9	−11	107.80	0
0.2822	8	3	11	−3	132.13	0	0.5597	11	10	21	−10	222.10	0	0.8699	8	15	23	−15	214.36	0
0.2883	13	5	18	−5	215.58	0	0.5629	12	11	23	−11	242.92	0	0.8759	13	3	13	−16	155.69	0
0.2979	1	3	3	1	48.18	0	0.5644	12	12	24	−11	253.25	0.2929	0.8993	1	2	3	−2	27.65	0
0.9196	15	4	15	−19	179.52	0	1.2803	10	10	15	−19	150.41	0.2505	1.6862	9	7	8	−16	100.24	0.2600
0.9269	11	3	11	−14	131.63	0	1.2803	15	4	10	−20	150.66	0.2505	1.6904	17	16	18	−33	205.86	0.2518
0.9308	7	15	22	−15	200.35	0	1.2830	16	9	16	−25	190.21	0	1.6944	9	8	9	−17	105.91	0
0.9358	6	13	19	−13	172.70	0	1.2851	17	14	22	−30	232.97	0.1611	1.7020	10	8	9	−18	111.94	0.2296
0.9380	13	15	26	−22	248.88	0.2114	1.2941	1	5	6	−5	48.03	0	1.7087	10	9	10	−19	117.63	0
0.9428	7	2	7	−9	83.75	0	1.3054	13	12	18	−24	185.83	0.1982	1.7149	11	9	10	−20	123.64	0.2056
0.9488	11	11	20	−18	194.36	0.2675	1.3089	12	7	12	−19	142.58	0	1.7203	11	10	11	−21	129.35	0
0.9530	4	9	13	−9	117.40	0	1.3150	17	10	17	−27	201.96	0	1.7255	12	10	11	−22	135.35	0.1860
0.9566	14	12	23	−22	229.04	0.2255	1.3184	3	16	19	−16	150.88	0	1.7301	12	11	12	−23	141.07	0
0.9602	10	3	10	−13	119.60	0	1.3297	5	3	5	−8	59.38	0	1.7344	13	11	12	−24	147.05	0.1699
0.9641	13	10	20	−20	202.25	0.2533	1.3405	3	17	20	−17	157.66	0	1.7344	12	12	13	−24	146.88	0.1699
0.9696	3	7	10	−7	89.76	0	1.3489	13	8	13	−21	154.32	0	1.7383	13	12	13	−25	152.79	0
0.9824	5	12	17	−12	151.86	0	1.3518	14	14	20	−27	203.56	0.1730	1.7420	14	12	13	−26	158.76	0.1563
1.0009	3	1	3	−4	35.86	0	1.3608	1	6	7	−6	54.81	0	1.7454	14	13	14	−27	164.51	0
1.0155	4	17	22	−14	190.69	0.2558	1.3710	12	13	18	−24	180.17	0.1922	1.7486	14	14	15	−28	170.33	0.1448
1.0186	5	13	18	−13	158.67	0	1.3750	11	7	11	−18	130.50	0	1.7515	15	14	15	−29	176.23	0
1.0248	17	6	17	−23	203.11	0	1.3832	14	9	14	−23	166.06	0	1.7516	16	13	14	−29	176.50	0.2791
1.0300	3	8	11	−8	96.56	0	1.3884	2	13	15	−13	116.41	0	1.7543	15	15	16	−30	182.05	0.1348
1.0346	14	12	22	−23	220.48	0.2171	1.3938	5	15	18	−18	148.39	0.2285	1.7569	16	15	16	−31	187.95	0
1.0379	11	4	11	−15	131.39	0	1.4130	3	2	3	−5	35.56	0	1.7570	15	16	17	−31	187.94	0.2605
1.0438	4	11	15	−11	131.02	0	1.4305	5	17	20	−20	161.63	0.2024	1.7593	17	15	16	−32	193.90	0.1261
1.0471	12	14	23	−22	219.13	0.2158	1.4350	2	15	17	−15	129.96	0	1.7616	17	16	17	−33	199.67	0
1.0518	8	3	8	−11	95.53	0	1.4391	16	11	16	−27	189.54	0	1.7617	16	17	18	−33	199.66	0.2442
1.0571	6	17	23	−17	199.93	0	1.4451	13	9	13	−22	153.98	0	1.8377	0	1	1	−1	6.77	0
1.0636	13	5	13	−18	155.21	0	1.4480	14	17	22	−30	215.83	0.1492	1.9190	17	16	15	−33	187.04	0.2288
1.0668	17	4	14	−22	185.97	0.2495	1.4548	1	8	9	−8	68.37	0	1.9191	16	17	16	−33	187.03	0
1.0825	1	3	4	−3	34.45	0	1.4622	17	12	17	−29	201.27	0	1.9217	16	16	15	−32	181.14	0.1179
1.0969	17	7	17	−24	202.85	0	1.4647	16	4	8	−21	146.01	0.2171	1.9244	16	15	14	−31	175.32	0.2430
1.0992	16	4	13	−21	173.73	0.2583	1.4728	7	5	7	−12	82.85	0	1.9245	15	16	15	−31	175.31	0
1.1029	12	5	12	−17	143.17	0	1.4805	17	4	8	−22	152.73	0.2049	1.9275	15	15	14	−30	169.42	0.1255
1.1108	5	16	21	−16	179.07	0	1.4891	1	9	10	−9	75.14	0	1.9306	15	14	13	−29	163.60	0.2591
1.1176	7	3	7	−10	83.49	0	1.4968	15	11	15	−26	177.44	0	1.9308	14	15	14	−29	163.59	0
1.1239	10	13	20	−20	187.06	0.2343	1.5000	14	2	5	−17	118.35	0.2593	1.9342	14	14	13	−28	157.70	0.1340
1.1285	3	10	13	−10	110.16	0	1.5000	5	12	14	−16	118.61	0.2593	1.9378	12	15	14	−27	152.16	0.2774
1.1328	12	14	22	−23	210.16	0.2070	1.5178	4	3	4	−7	47.29	0	1.9380	13	14	13	−27	151.87	0
1.1371	9	4	9	−13	107.31	0	1.5339	16	2	5	−19	131.89	0.2260	1.9419	13	13	12	−26	145.98	0.1439
1.1422	11	11	18	−20	176.84	0.2434	1.5364	17	13	17	−30	200.90	0	1.9461	11	14	13	−25	140.46	0.2985
1.1495	2	7	9	−7	75.70	0	1.5421	1	11	12	−11	88.68	0	1.9464	12	13	12	−25	140.15	0
1.1554	15	13	22	−26	223.82	0.1901	1.5529	9	7	9	−16	106.31	0	1.9510	12	12	11	−24	134.26	0.1553

TABLE II. *(Continued.).*

θ (deg)	n_1^α	n_2^α	n_1^β	n_2^β	L^{SM}	ΔL	θ (deg)	n_1^α	n_2^α	n_1^β	n_2^β	L^{SM}	ΔL	θ (deg)	n_1^α	n_2^α	n_1^β	n_2^β	L^{SM}	ΔL
1.1581	13	6	13	−19	154.94	0	1.5630	1	12	13	−12	95.46	0	1.9563	11	12	11	−23	128.43	0
1.1645	15	7	15	−22	178.75	0	1.5697	6	16	18	−21	149.61	0.1929	1.9619	10	12	11	−22	122.70	0.1687
1.1693	3	11	14	−11	116.95	0	1.5811	5	4	5	−9	59.02	0	1.9682	10	11	10	−21	116.71	0
1.1788	4	15	19	−15	158.20	0	1.5970	1	14	15	−14	108.99	0	1.9750	10	10	9	−20	110.81	0.1845
1.1820	6	16	21	−18	179.34	0.2313	1.6042	11	9	11	−20	129.76	0	1.9828	9	10	9	−19	104.99	0
1.2056	2	1	2	−3	23.81	0	1.6110	1	15	16	−15	115.76	0	1.9913	9	9	8	−18	99.08	0.2037
1.2303	4	17	21	−17	171.78	0	1.6235	6	5	6	−11	70.74	0	2.0011	8	9	8	−17	93.27	0
1.2335	2	16	19	−14	151.75	0.2601	1.6346	1	17	18	−17	129.30	0	2.0064	16	17	15	−33	180.60	0.2209
1.2382	3	13	16	−13	130.53	0	1.6398	13	11	13	−24	153.21	0	2.0119	8	8	7	−16	87.36	0.2272
1.2420	17	9	17	−26	202.27	0	1.6538	7	6	7	−13	82.47	0							
1.2469	15	8	15	−23	178.46	0	1.6660	15	13	15	−28	176.66	0							
1.2532	2	9	11	−9	89.28	0	1.6663	8	6	7	−14	88.54	0.2996							
1.2584	13	15	22	−26	212.97	0.1809	1.6715	16	13	15	−29	182.69	0.2888							
1.2619	11	6	11	−17	130.83	0	1.6766	8	7	8	−15	94.19	0							
1.2675	3	14	17	−14	137.32	0	1.6815	16	15	17	−31	194.13	0.2691							
1.2744	9	5	9	−14	107.01	0	1.6860	17	15	17	−32	200.10	0							

[1] J. M. B. Lopes dos Santos, N. M. R. Peres, and A. H. Castro Neto, Phys. Rev. Lett. **99**, 256802 (2007).

[2] E. J. Mele, Phys. Rev. B **81**, 161405(R) (2010).

[3] G. Trambly de Laissardière, D. Mayou, and L. Magaud, Nano Lett. **10**, 804 (2010).

[4] S. Shallcross, S. Sharma, E. Kandelaki, and O. A. Pankratov, Phys. Rev. B **81**, 165105 (2010).

[5] E. Suárez Morell, J. D. Correa, P. Vargas, M. Pacheco, and Z. Barticevic, Phys. Rev. B **82**, 121407(R) (2010).

[6] R. Bistritzer and A. MacDonald, Proc. Natl. Acad. Sci. U.S.A. **108**, 12233 (2011).

[7] P. Moon and M. Koshino, Phys. Rev. B **85**, 195458 (2012).

[8] G. Trambly de Laissardière, D. Mayou, and L. Magaud, Phys. Rev. B **86**, 125413 (2012).

[9] Y. Cao, V. Fatemi, S. Fang, K. Watanabe, T. Taniguchi, E. Kaxiras, and P. Jarillo-Herrero, Nature (London) **556**, 43 (2018).

[10] Y. Cao, V. Fatemi, A. Demir, S. Fang, S. L. Tomarken, J. Y. Luo, J. D. Sanchez-Yamagishi, K. Watanabe, T. Taniguchi, E. Kaxiras, R. C. Ashoori, and P. Jarillo-Herrero, Nature (London) **556**, 80 (2018).

[11] M. Yankowitz, S. Chen, H. Polshyn, Y. Zhang, K. Watanabe, T. Taniguchi, D. Graf, A. F. Young, and C. R. Dean, Science **363**, 1059 (2019).

[12] X. Lu, P. Stepanov, W. Yang, M. Xie, M. A. Aamir, I. Das, C. Urgell, K. Watanabe, T. Taniguchi, G. Zhang, A. Bachtold, A. H. MacDonald, and D. K. Efetov, Nature (London) **574**, 653 (2019).

[13] C. Dean, A. Young, I. Meric, C. Lee, L. Wang, S. Sorgenfrei, K. Watanabe, T. Taniguchi, P. Kim, K. Shepard, and J. Hone, Nat. Nanotechnol. **5**, 722 (2010).

[14] M. Kindermann, B. Uchoa, and D. L. Miller, Phys. Rev. B **86**, 115415 (2012).

[15] J. R. Wallbank, A. A. Patel, M. Mucha-Kruczyński, A. K. Geim, and V. I. Fal'ko, Phys. Rev. B **87**, 245408 (2013).

[16] M. Mucha-Kruczyński, J. R. Wallbank, and V. L. Fal'ko, Phys. Rev. B **88**, 205418 (2013).

[17] J. Jung, A. Raoux, Z. Qiao, and A. H. MacDonald, Phys. Rev. B **89**, 205414 (2014).

[18] P. Moon and M. Koshino, Phys. Rev. B **90**, 155406 (2014).

[19] C. Dean, L. Wang, P. Maher, C. Forsythe, F. Ghahari, Y. Gao, J. Katoch, M. Ishigami, P. Moon, M. Koshino, T. Taniguchi, K. Watanabe, K. Shepard, J. Hone, and P. Kim, Nature (London) **497**, 598 (2013).

[20] L. A. Ponomarenko, R. V. Gorbachev, G. L. Yu, D. C. Elias, R. Jalil, A. A. Patel, A. Mishchenko, A. S. Mayorov, C. R. Woods, J. R. Wallbank, M. Mucha-Kruczynski, B. A. Piot, M. Potrefemski, I. V. Grigorieva, K. S. Novoselov, F. Guinea, V. I. Fal'ko, and A. K. Geim, Nature (London) **497**, 594 (2013).

[21] B. Hunt, J. Sanchez-Yamagishi, A. Young, M. Yankowitz, B. LeRoy, K. Watanabe, T. Taniguchi, P. Moon, M. Koshino, P. Jarillo-Herrero, and R. Ashoori, Science **340**, 1427 (2013).

[22] G. L. Yu, R. V. Gorbachev, J. S. Tu, A. V. Kretinin, Y. Cao, R. Jalil, F. Withers, L. A. Ponomarenko, B. A. Piot, M. Potemski, D. C. Elias, X. Chen, K. Watanabe, T. Taniguchi, I. V. Grigorieva, K. S. Novoselov, V. I. Fal'ko, A. K. Geim, and A. Mishchenko, Nat. Phys. **10**, 525 (2014).

[23] N. R. Finney, M. Yankowitz, L. Muraleetharan, K. Watanabe, T. Taniguchi, C. R. Dean, and J. Hone, Nat. Nanotechnol. **14**, 1029 (2019).

[24] L. Wang, S. Zihlmann, M.-H. Liu, P. Makk, K. Watanabe, T. Taniguchi, A. Baumgartner, and C. Schönenberger, Nano Lett. **19**, 2371 (2019).

[25] Z. Wang, Y. B. Wang, J. Yin, E. Tóvári, Y. Yang, L. Lin, M. Holwill, J. Birkbeck, D. Perello, S. Xu, *et al.*, Sci. Adv. **5**, eaay8897 (2019).

[26] Y. Yang, J. Li, J. Yin, S. Xu, C. Mullan, T. Taniguchi, K. Watanabe, A. K. Geim, K. S. Novoselov, and A. Mishchenko, Sci. Adv. **6**, eabd3655 (2020).

[27] M. Andelkovic, S. P. Milovanovic, L. Covaci, and F. M. Peeters, Nano Lett. **20**, 979 (2020).

[28] N. Leconte and J. Jung, 2D Mater. **7**, 031005 (2020).

[29] M. Onodera, K. Kinoshita, R. Moriya, S. Masubuchi, K. Watanabe, T. Taniguchi, and T. Machida, Nano Lett. **20**, 4566 (2020).

[30] M. Kuiri, S. K. Srivastav, S. Ray, K. Watanabe, T. Taniguchi, T. Das, and A. Das, Phys. Rev. B **103**, 115419 (2021).

[31] J. Shi, J. Zhu, and A. H. MacDonald, Phys. Rev. B **103**, 075122 (2021).

[32] J. Shin, Y. Park, B. L. Chittari, J.-H. Sun, and J. Jung, Phys. Rev. B **103**, 075423 (2021).

[33] X. Huang, L. Chen, S. Tang, C. Jiang, C. Chen, H. Wang, Z.-X. Shen, H. Wang, and Y.-T. Cui, arXiv:2102.08594.

[34] Z. Zhu, S. Carr, D. Massatt, M. Luskin, and E. Kaxiras, Phys. Rev. Lett. **125**, 116404 (2020).

[35] F. Lin, J. Qiao, J. Huang, J. Liu, D. Fu, A. S. Mayorov, H. Chen, P. Mukherjee, T. Qu, C.-H. Sow, *et al.*, Nano Lett. **20**, 7572 (2020).

[36] J. M. Park, Y. Cao, K. Watanabe, T. Taniguchi, and P. Jarillo-Herrero, Nature (London) **590**, 249 (2021).

[37] Z. Hao, A. Zimmerman, P. Ledwith, E. Khalaf, D. H. Najafabadi, K. Watanabe, T. Taniguchi, A. Vishwanath, and P. Kim, Science **371**, 1133 (2021).

[38] A. Kitaev, in *Advances in Theoretical Physics: Landau Memorial Conference*, AIP Conf. Proc. No. 1134 (AIP, Melville, NY, 2009), p. 22.

[39] J. C. Y. Teo and C. L. Kane, Phys. Rev. B **82**, 115120 (2010).

[40] Y. Xu, F. Zhang, and C. Zhang, Phys. Rev. Lett. **115**, 265304 (2015).

[41] D. J. Thouless, Phys. Rev. B **27**, 6083 (1983).

[42] Q. Niu, Phys. Rev. B **34**, 5093 (1986).

[43] Y. E. Kraus, Y. Lahini, Z. Ringel, M. Verbin, and O. Zilberberg, Phys. Rev. Lett. **109**, 106402 (2012).

[44] M. Fujimoto, H. Koschke, and M. Koshino, Phys. Rev. B **101**, 041112(R) (2020).

[45] D. J. Thouless, M. Kohmoto, M. P. Nightingale, and M. den Nijs, Phys. Rev. Lett. **49**, 405 (1982).

[46] S. J. Ahn, P. Moon, T.-H. Kim, H.-W. Kim, H.-C. Shin, E. H. Kim, H. W. Cha, S.-J. Kahng, P. Kim, M. Koshino, *et al.*, Science **361**, 782 (2018).

[47] P. Moon, M. Koshino, and Y.-W. Son, Phys. Rev. B **99**, 165430 (2019).

[48] J. A. Crosse and P. Moon, Phys. Rev. B **103**, 045408 (2021).

[49] H. Ha and B.-J. Yang, arXiv:2103.08851.

[50] L. Liu, Y. P. Feng, and Z. Z. Shen, Phys. Rev. B **68**, 104102 (2003).

[51] M. Koshino, New J. Phys. **17**, 015014 (2015).

[52] D. Hofstadter, Phys. Rev. B **14**, 2239 (1976).

[53] P. G. Harper, Proc. Phys. Soc. London, Sect. A **68**, 879 (1955).

[54] S. Aubry and G. André, Ann. Isr. Phys. Soc. **3**, 133 (1980).

[55] W. Steurer and S. Deloudi, *Crystallography of Quasicrystals: Concepts, Methods and Structures*, Vol. 126 in Springer Series in Materials Science (Springer-Verlag, Berlin, Heidelberg, 2009).

[56] N. W. Ashcroft and N. D. Mermin, *Solid State Physics* (Saunders College, Philadelphia, 1976).

[57] A. P. Smith and N. W. Ashcroft, Phys. Rev. Lett. **59**, 1365 (1987).

[58] J.-M. Gambaudo and P. Vignolo, New J. Phys. **16**, 043013 (2014).

[59] M. Yoshii, S. Kitamura, and T. Morimoto, arXiv:2105.05654.

[60] Y. Zhang, Y. Gao, and D. Xiao, Phys. Rev. B **101**, 041410(R) (2020).

[61] Y. Su and S.-Z. Lin, Phys. Rev. B **101**, 041113(R) (2020).